applied sciences

MDPI

Review

Atomic and Electronic Structure of Metal–Salen Complexes [M(Salen)], Their Polymers and Composites Based on Them with Carbon Nanostructures: Review of X-ray Spectroscopy Studies

Petr M. Korusenko [1,2,*], Olga V. Petrova [1,3] and Alexander S. Vinogradov [1]

[1] Department of Solid State Electronics, V.A. Fock Institute of Physics, St. Petersburg State University, 7/9 Universitetskaya nab., 199034 Saint Petersburg, Russia; asvinograd@gmail.com (A.S.V.)
[2] Department of Physics, Omsk State Technical University, 11 Mira prosp., 644050 Omsk, Russia
[3] Institute of Physics and Mathematics, Komi Science Centre, Ural Branch of the Russian Academy of Sciences, 167982 Syktyvkar, Russia
* Correspondence: korusenko_petr@mail.ru

Abstract: Currently, electrically conductive polymers based on transition metal complexes [M(Salen)], as well as their composites, are among the systems showing promise as catalysts, electrochromic and electroluminescent materials, and electrodes for energy storage (for batteries and supercapacitors). The current review focuses on elucidating the atomic and electronic structure of metal–salen complexes, their polymers, and composites with nanostructured carbon (carbon nanotubes and graphene) using modern X-ray spectroscopy methods (X-ray photoelectron (XPS) and valence-band photoemission (VB PES) spectroscopy, as well as near-edge (NEXAFS) and extended (EXAFS) X-ray absorption fine structure spectroscopy). We trust that this review will be of valuable assistance to researchers working in the field of synthesizing and characterizing metal–salen complexes and composites based on them.

Keywords: [M(Salen)]-based materials; polymers; carbon nanotubes; graphene and graphene oxide (GO); composites; atomic and electronic structure; X-ray photoelectron; valence-band photoemission (XPS and VB PES) spectroscopy; X-ray absorption (NEXAFS and EXAFS) spectroscopy

Citation: Korusenko, P.M.; Petrova, O.V.; Vinogradov, A.S. Atomic and Electronic Structure of Metal–Salen Complexes [M(Salen)], Their Polymers and Composites Based on Them with Carbon Nanostructures: Review of X-ray Spectroscopy Studies. *Appl. Sci.* **2024**, *14*, 1178. https://doi.org/10.3390/app14031178

Academic Editor: Philippe Lambin

Received: 30 December 2023
Revised: 19 January 2024
Accepted: 26 January 2024
Published: 30 January 2024

1. Introduction

The discovery at the end of the last century of polymer materials whose conductivity is only slightly lower than that of metals has stimulated a large amount of basic and applied research, which is expected to lead to the development of new electronic and photoelectric devices, including nanoscale ones [1]. Polymers electrochemically synthesized from the monomeric planar complexes of 3*d*-atoms with such ligands as porphyrin, phthalocyanine, Schiff base, etc., are particularly interesting due to the presence of a number of unique properties. The polymers of square–planar complexes of 3*d* metal (M) atoms with tetradentate N_2O_2 Schiff base ligands, the so-called salen complexes ([M(Salen)]), are characterized by high redox conductivity, electrochromic behavior, and selective catalytic activity in heterogeneous reactions (including electrocatalysis) [2]. An important advantage of these polymers is also their high thermal stability (up to 350 °C) compared with monomer complexes due to their conductive polymer matrix. It is also expected that the synthesis of nanocomposites based on poly-[M(Salen)] and various forms of carbon (mesoporous and activated carbon), including nanostructured ones (carbon nanotubes, graphene, and nanoglobular carbon), will lead to the development of materials with improved energetic, catalytic, and other characteristics [3–10]. This quality improvement is achieved due to the uniform distribution of the polymer on the surface of the carbon component of the composite material, which has a high specific surface area, electrical conductivity, and mechanical properties (strength, elasticity).

In the past two decades, all these problems have been the subject of large-scale research on redox poly-[M(Salen)] and their composites [1,2,11–44]. Until now, the most popular methods for experimentally characterizing the properties of these new materials remain scanning electron microscopy (SEM), *in situ* UV–visible and IR spectroscopy, *in situ* ellipsometry, and electrochemical methods (cyclic voltammetry, chronoamperometry, impedance spectroscopy, etc.) [3–16]. However, the methods used provide far from a complete understanding and description of the formation processes of these systems. First of all, this concerns the lack of important information about the spatial localization and atomic orbital composition of the upper occupied and lower unoccupied molecular orbitals (MOs) of monomer complexes, since electronic transitions between these MOs determine the chemical bonding of monomers during their polymerization. At the same time, these transitions often occur between MOs localized on different metal and ligand atoms of the complex and are therefore associated with the charge transfer between them. All of this makes it difficult to fully understand and correctly describe the electronic properties of these complexes, which are of particular importance for their practical use.

Thus, for the widespread use in modern technologies of electrically conductive redox poly-[M(Salen)] polymers and their composites with carbon nanostructures, detailed knowledge is required about the properties of occupied and empty valence MOs of complexes, which are responsible for processes of electrochemical polymerization of monomers and the mechanisms of redox conductivity in these polymer compounds.

The X-ray transitions of inner-shell electrons are different from valence electronic transitions probed by optical absorption spectroscopy since they are element-specific, atomically localized transitions. Therefore, the X-ray absorption and photoelectron spectroscopy methods are among the most informative experimental techniques for studying the local atomic and electronic structures of various polyatomic systems: molecules, complexes, polymers, etc. However, recent studies are characterized by only separate attempts to use the methods of X-ray core-level photoelectron spectroscopy (XPS) [8,26,35,37,39,40,42–52] and valence-band photoemission spectroscopy (VB PES) [45,46,53], as well as X-ray absorption spectroscopy (near-edge X-ray absorption fine structure, NEXAFS, and extended X-ray absorption fine structure, EXAFS) [27,29,30,40,45,46,52–56] to obtain information about the features of the electronic structure of [M(Salen)] complexes, their polymers, and composites based on them, as well as about the atomic structure of these polyatomic systems.

The main purpose of this review is to summarize the existing knowledge on the use of X-ray spectroscopy methods (XPS, VB PES, NEXAFS, EXAFS) to characterize the atomic–electronic structure of [M(Salen)] complexes, their polymers, and their composites with carbon nanostructures.

2. [M(Salen)] Complexes, Their Polymers, and Composites Based Thereon

This section discusses in detail the structure and methods of preparation of various [M(Salen)] complexes, their polymers, and composites with carbon nanostructures such as carbon nanotubes and graphene.

2.1. Structure and Methods for Preparing [M(Salen)] Complexes and Their Polymers

2.1.1. Monomeric Complexes

Schiff bases derived from salicylic aldehyde and its derivatives, specifically N,N′-ethylene-bis(salicylimine), $C_{16}H_{16}N_2O_2$ or H_2(Salen), commonly referred to as the salen ligand, are widely used in practical applications (Figure 1). The salen ligand consists of two C_6H_5OH phenolic groups linked by an ethylenediamine bridge of –N–C(H_2)–C(H_2)–N– and is formed by combining two equivalents of salicylic aldehyde with one equivalent of ethylenediamine. The structure of the molecule consists of several isomers, which differ in the position of the two hydrogen atoms and also in the mutual orientation of the two benzene moieties. Density functional theory (DFT) calculations reveal that the most energetically favorable isomer features a C_2 symmetry configuration and two phenolic groups [57]. It was demonstrated that the energy stabilization of this isomer is a result

of two strong intramolecular N···H hydrogen bonds. Furthermore, the out-of-plane distortion of benzene moieties in all isomers is negligible.

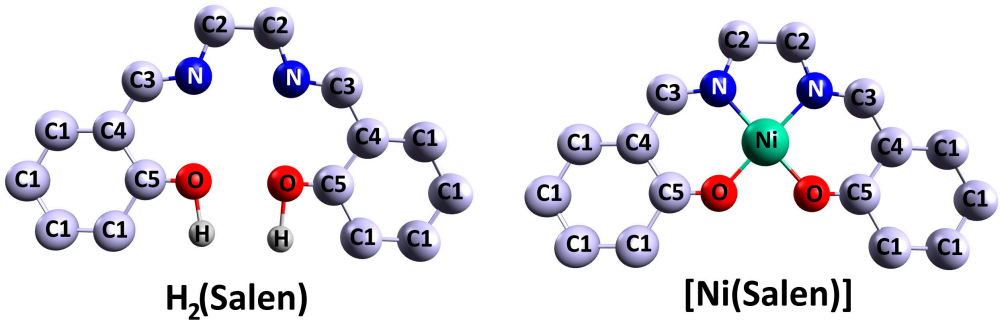

Figure 1. Schematic illustration of the H_2(Salen) salen ligand and [Ni(Salen)] molecular complex [46].

Let us consider the structure of [M(Salen)] complexes (M = transition metal such as V, Cr, Mn, Fe, Co, Ni, Cu, Pd) using the example of the monomer N,N′-ethylene-bis(salicylaldiminato)nickel(II), $NiO_2N_2C_{16}H_{14}$ (hereafter [Ni(Salen)]). The [Ni(Salen)] is considered a standard representation of complex 3*d*-atom monomers with Schiff bases [M(Schiff)] (Figure 1) [18,45,58,59]. The molecule consists of a nickel atom bound to a tetradentate N_2O_2 ligand of the salen type forming an almost planar coordination center [NiN_2O_2] with C_{2v} symmetry. Geometrically, it is close to a square, since the interatomic distances R (Ni–O) = 1.882 Å and R (Ni–N) = 1.889 Å are close to each other [18]. Two C_6H_5O-phenyl groups are located at the periphery of the ligand. The square–planar symmetry of [M(Salen)] complexes and the [MN_2O_2] donor coordination center present in them enable the complexes to be involved in various types of intermolecular interactions and in the formation of supramolecular structures.

Currently, it is possible to prepare [M(Salen)] complexes using (i) metal alkoxides ($M(OR)_n$), (ii) metal amides $M(NMe_2)_4$, (iii) a two-step reaction involving deprotonation of Schiff bases using lithium bases (CH_3Li, C_4H_9Li) and sequential reaction with metal halides, (iv) alkyl metal complexes $M(CH_3)$, and (v) $M(OAc)_2$ metal acetates through heating a Schiff base in the presence of a metal salt under boiling conditions [45,46,49–51].

Considerable attention has been given lately to the synthesis and analysis of new coordination compounds based on [M(Salen)], in which the environment of the metal atom M has been modified by the addition of atomic groups chemically bonded to the salen ligand atoms or to the metal atom. This modification enables the advancement of electroactive photosensitive materials, including nanocomposites, towards higher efficiency [14,25,26,30,32,34,35].

2.1.2. Polymers Prepared by Electropolymerization of [M(Salen)] Monomeric Molecules

The first studies of polymers based on transition metal complexes with salen-type Schiff ligands were largely focused on characterizing electrochemical methods for obtaining conducting polymer layers on an electrode from monomers and studying the conductive properties of the resulting polymers using electrometric methods depending on the solvent and type of ligand. It was demonstrated in [19,20] that these complexes are reversibly oxidized in strong-donor solvents and oxidatively polymerized in solvents with weak donors. The monomers' oxidation mechanisms were analyzed using cyclic voltammetry and scanning electron microscopy. It has been shown that the polymer layer's thickness on the electrode increases linearly over several voltammetric scans. Also, the initial growth rate of the polymer layer increases linearly with rising monomer concentration in the electrolyte solution.

Despite a significant amount of research into the structure and properties of electrically conductive redox polymers poly-[M(Salen)], and in particular poly-[Ni(Salen)], there is no consensus on the mechanism of polymerization of monomer molecules [1,2,11–16,19–21,23–35,40–43]. The first model assumes chemical linkage between the phenyl groups of the ligands of

neighboring molecules (chainlike structure). In this instance, the polymer forms through the formation of covalent C–C bonds between carbon atoms in the para positions of the phenyl moieties (Figure 2a) and is inherently purely liganded. [19,24]. The second model of the polymerization mechanism is based on processes associated with the metal atom, which we will consider using the example of nickel [21,60]. In this case, the complexing nickel cation Ni(II) is first additionally oxidized Ni(II) → Ni(III) + e^-. Subsequently, it can form a stacklike structure which is stabilized by chemical bonding (and charge transfer) between the nickel cation and the phenyl moieties of neighboring monomer molecules (as shown in Figure 2b). Finally, the third model combines the two previous ones: the electro-oxidation of monomers leads to the formation of stacklike structures. These structures are then cross-linked through the formation of covalent C–C bonds, leading to the appearance of π-conjugated chains involving the phenyl rings of the ligand (Figure 2c) [21,60].

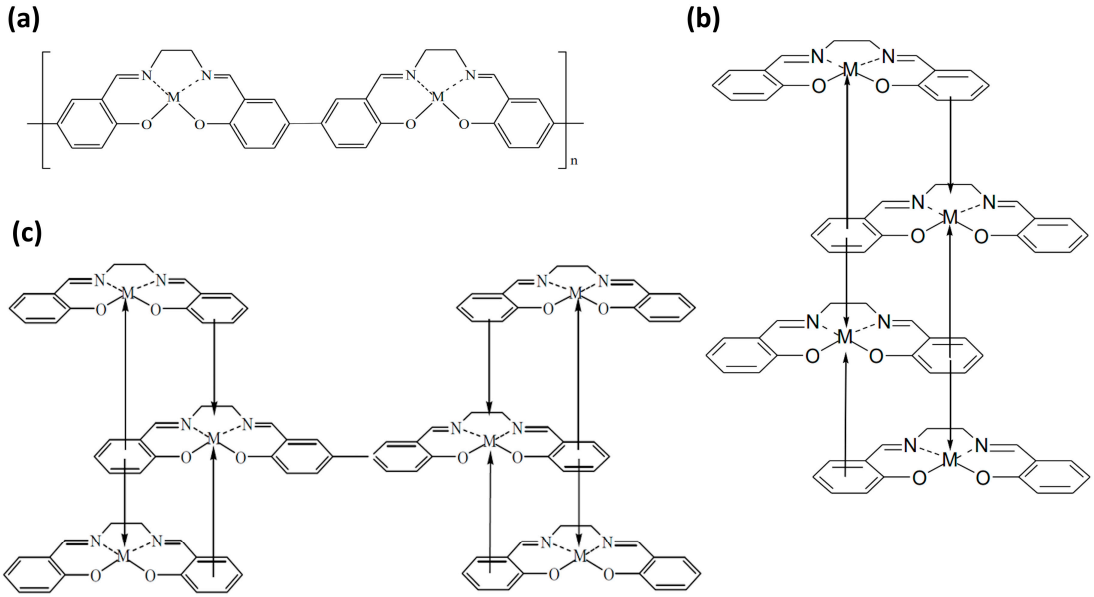

Figure 2. Models of poly-[M(Salen)] structure: (**a**) chain-like structure; (**b**) stack-like structure; and (**c**) hybrid variant.

Over the past 20 years, two contrasting viewpoints regarding the electrochemical activity of conducting polymers have been significantly discussed, in which two options are considered as redox positions (places where redox reactions occur): cations of metal atoms [20,21] or ligand atoms [22,23]. Over these two decades, different groups of researchers have studied salen complexes and polymers based on them using voltammetry and chronoamperometry [11,12], *in situ* UV–vis and IR spectroscopy [11,13], *in situ* ellipsometry [12], electrochemical quartz microbalances [12,14,15], and impedance spectroscopy [16]. Both mechanisms are characterized by different charge transfer in [Ni(Salen)] and, as a consequence, different charge states of Ni, N, O, and C atoms in the reduced (neutral) and oxidized states of poly-[Ni(Salen)]. To directly identify nickel atoms in a highly oxidized state within redox polymers, the electron paramagnetic resonance (EPR) technique was used [12,14,23,24,40]. The conducted measurements did not detect highly oxidized Ni(III) atoms within the polymer. This led the authors of these studies to choose the first model, based on the processes of oxidation and reduction of ligands, for the mechanism of polymerization and electrochemical activity of polymers. In [21], it was also suggested that the polymerization mechanism of [M(Salen)] monomer molecules, involving a metal cation, could occasionally be accompanied by the direct linking of ligands from different monomer molecules (the first model of polymerization). Nevertheless, the results of all these studies did not provide sufficient evidence to make a conclusive decision regarding the polymerization mechanism models described.

Electropolymerization of monomeric [M(Salen)] molecules is usually performed using potentiostatic and potentiodynamic methods, as well as galvanostatic charging [61]. The polymer film thickness of poly-[M(Salen)] can be easily controlled by the polymerization charge (for potentiostatic methods) or the number of charge–discharge cycles (for potentiodynamic methods) [61]. In addition, layer-by-layer polymerization of metal salens is also possible [62].

2.2. Preparation of Composites Based on [M(Salen)] and Carbon Nanomaterials

Carbon materials have found applications in many fields of science, industry, medicine, etc., due to the variety of allotropic forms with unique physical and chemical properties [63]. At the same time, the discovery of 0D, 1D, and 2D carbon nanomaterials such as fullerenes, carbon nanotubes (CNTs), and graphene marked a breakthrough in materials science and nanotechnology. It should be noted that carbon nanomaterials have become widespread not only as an independent functional material but also as a basis or modifying additive for the preparation of composites with metal compounds, polymers, biomolecules, etc. In this review section, carbon nanotubes and graphene are considered to be the most widely used in the preparation of composites based on [M(Salen)] complexes and carbon nanomaterials.

2.2.1. Nanotubes and Graphene as a Promising Basis for Composites

CNTs and graphene have attracted considerable attention due to their exceptional surface area and impressive electrical, mechanical, thermal, and chemical properties. These materials have diverse applications, such as catalysis, sensor technologies, and energy storage and conversion. Additionally, they offer significant potential for use in solar cells and fuel cells [64–67]. Table 1 presents a summary of the essential properties of these materials for comparative analysis.

Table 1. Comparison of physical properties for some carbon nanomaterials.

Material	Specific Surface Area, m^2g^{-1}	Young's Modulus, TPa	Thermal Conductivity (at Room Temperature), $Wm^{-1}K^{-1}$	Refs.
SWCNTs	400–900	~1	3000	[68]
MWCNTs	200–400	0.3–1	3000	[68]
Monolayer graphene	up to 2630	1	5000	[69–71]
rGO sheet	up to 713	0.25	46.1 to 118.7	[69,70,72]
Freestanding GO	up to 456	0.7 ± 0.015	72 (oxidation degree of 0.35); 670 (oxidation degree of 0.05)	[69,70,73]

CNTs are a type of carbon allotrope, which were discovered by Iijima [74]. These 1D, nanoscale, hollow cylinders are formed by rolling up a hexagonal lattice of sp^2-hybridized carbon atoms without any seams [75–78].

CNTs measure a few microns in length and have a nanosized outer diameter, resulting in a large aspect ratio. Depending on the number of rolled-up graphene layers, they can be categorized as single-walled (SWCNTs) (outer diameter ~1–2 nm) and multiwalled (MWCNTs) (outer diameter ~2–50 nm), with interlayer spacing in the range of 0.32–0.35 nm [75,79]. There are three main nanotube configurations for SWCNTs depending on the chirality vector (C_h), i.e., the direction along which the graphene sheet is rolled up: armchair, zigzag, and chiral (Figure 3a). It is the chirality that predetermines the electrical, mechanical, optical, and other properties of CNTs [75]. Therefore, SWCNTs can exhibit both metallic and semiconductor conductivity depending on chirality, whereas MWCNTs only exhibit metallic conductivity. MWCNTs are able to take on different shapes, including a Russian doll made of several concentric graphene tubes, a scroll-type structure created by wrapping a single graphene sheet, and a bamboo-shaped structure (Figure 3b) [80,81]. Significantly, the multilayered structure of MWCNTs enables the outer layer not only to

protect the inner tubes from chemical reactions during environmental interactions but also to manifest superior tensile properties, which was a disadvantage of SWCNTs [80]. CNTs can be obtained by using the following different methods: arc discharge, laser ablation, chemical vapor deposition (CVD), plasma-enhanced CVD, liquid pyrolysis, solid-state pyrolysis, flame pyrolysis, bottom-up organic approach, etc. [80,82,83].

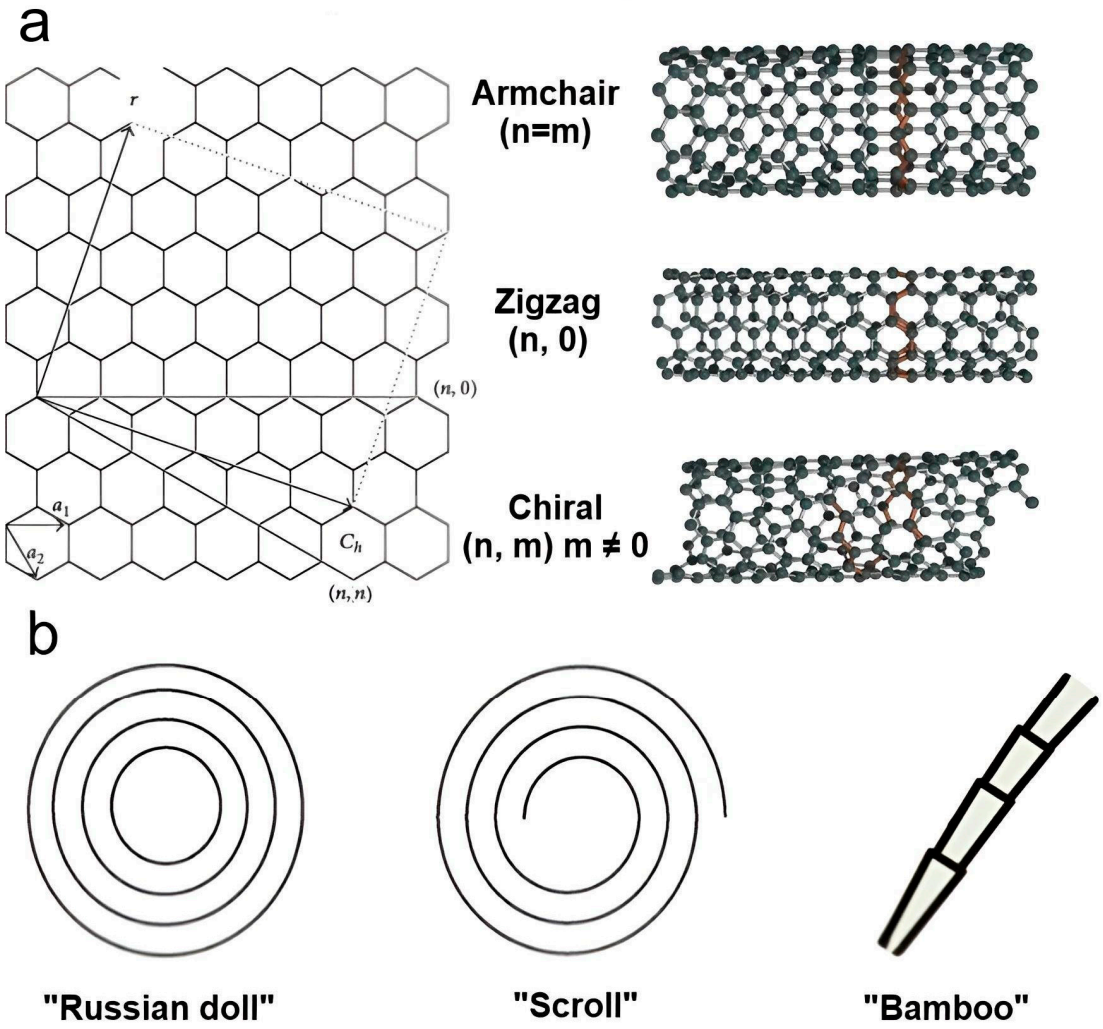

Figure 3. The main types of carbon nanotubes: (**a**) variants of SWCNTs constructed from a graphene sheet along the chiral vector C_h and (**b**) various forms of MWCNTs.

Graphene is a 2D allotrope of carbon, first discovered by Geim and Novoselov in 2004 [84]. It is a single layer of carbon atoms linked by sp^2 hybridized bonds to form a hexagonal two-dimensional crystal lattice (Figure 4a). There are also bilayer graphene and few-layer graphene, which are formed from multiple graphene sheets held together by strong π-π interactions (Figure 4a) [85–88]. The complexity of the actual structure of graphene sheets is much more complex due to the presence of edge regions [88]. They are intricate chemical compounds consisting mainly of oxygen-containing functional groups, such as carboxylates, carbonyls, hydroxyl, epoxy, alkoxy groups, etc. (Figure 4a) [89,90]. The presence of these groups on the edges of graphene function as attachment sites for active particles, polymers, and biomolecules during the formation of composites [91–93].

Additionally, when preparing graphene-based composites, point and extended structural defects arise in the hexagonal graphene lattice, leading to a significant increase in the number of attachment sites for active particles [94,95]. Graphene can be obtained through various procedures including epitaxy; CVD; physical exfoliation of graphite; chemical treatment of graphite to form graphene oxide (GO) through oxidative exfoliation of graphite

followed by reduction of GO to form reduced GO (rGO) (Figure 4b); and others. Each of the aforementioned methods offers a unique level of control over the structure and purity of the obtained graphene, enabling its use in specific areas of science and technology [91,96]. Due to their distinctive structure, both CNTs and graphene are two nanomaterials with significant values of optical, thermal, mechanical, and electronic properties. For this reason, they are widely used in the development of new functional composites with improved properties [97–99].

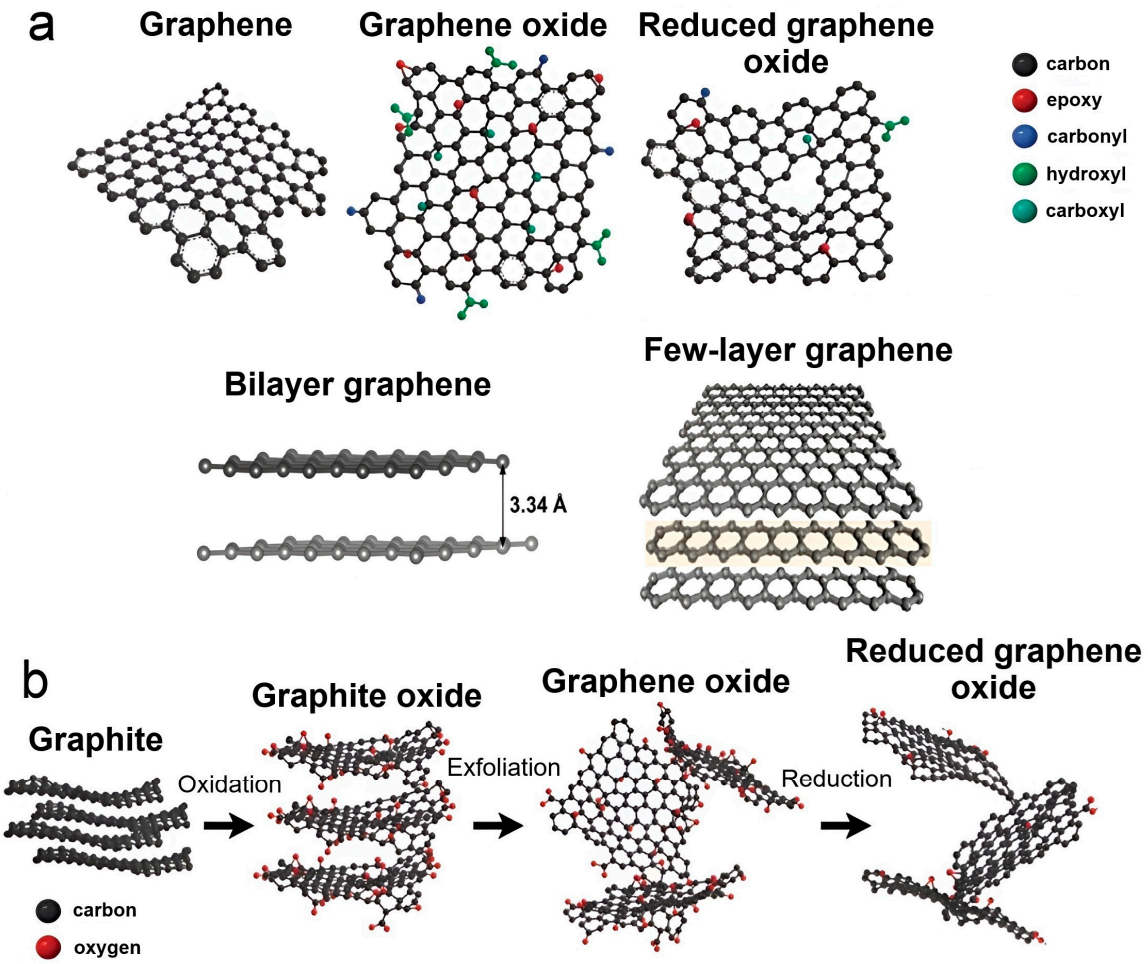

Figure 4. Possible types of graphene and representation of the process of obtaining reduced graphene oxide by oxidative exfoliation of graphite. (**a**) Types of graphene and the main oxygen-containing functional groups on its edges; (**b**) Scheme for obtaining reduced GO from graphite by chemical treatment.

2.2.2. Features of the Formation of [M(Salen)]/Carbon Nanotubes and [M(Salen)]/Graphene Composites

Currently, preparing composites based on [M(Salen)] complexes and CNTs or graphene remains a challenging and unsolved problem. This is primarily attributed to the ultrasmooth surfaces of both CNTs and graphene, which exhibit few broken bonds or structural defects, with the exception of the edges of graphene or the tips of nanotubes [97,98]. Without pretreatment (functionalization), CNT or graphene surfaces tend to bind easily due to strong van der Waals interactions between individual nanostructures, resulting in the formation of poorly dispersed bundles or agglomerates. As a result, poor interfacial interaction between the components of the composite is observed, which seriously impairs its characteristics. To solve this problem, there are methods based on noncovalent (due to electrostatic interactions or physical adsorption) and covalent functionalization (with the formation of stable chemical bonds) of the CNT or graphene surface. Noncovalent functionalization techniques can improve the dispersion quality of carbon nanomaterials

in solution. However, they do not address the challenges of interphase interactions at composite interfaces. Covalent functionalization is a more sought-after way of forming composites and is usually obtained by direct reaction of the metal complex with the surface groups of the carbon material or by a spacer (a chain of atoms linking a functional group on the surface of the carbon material and the metal complex) pregrafted onto the carbon material or onto the [M(Salen)] complex (Figure 5) [57].

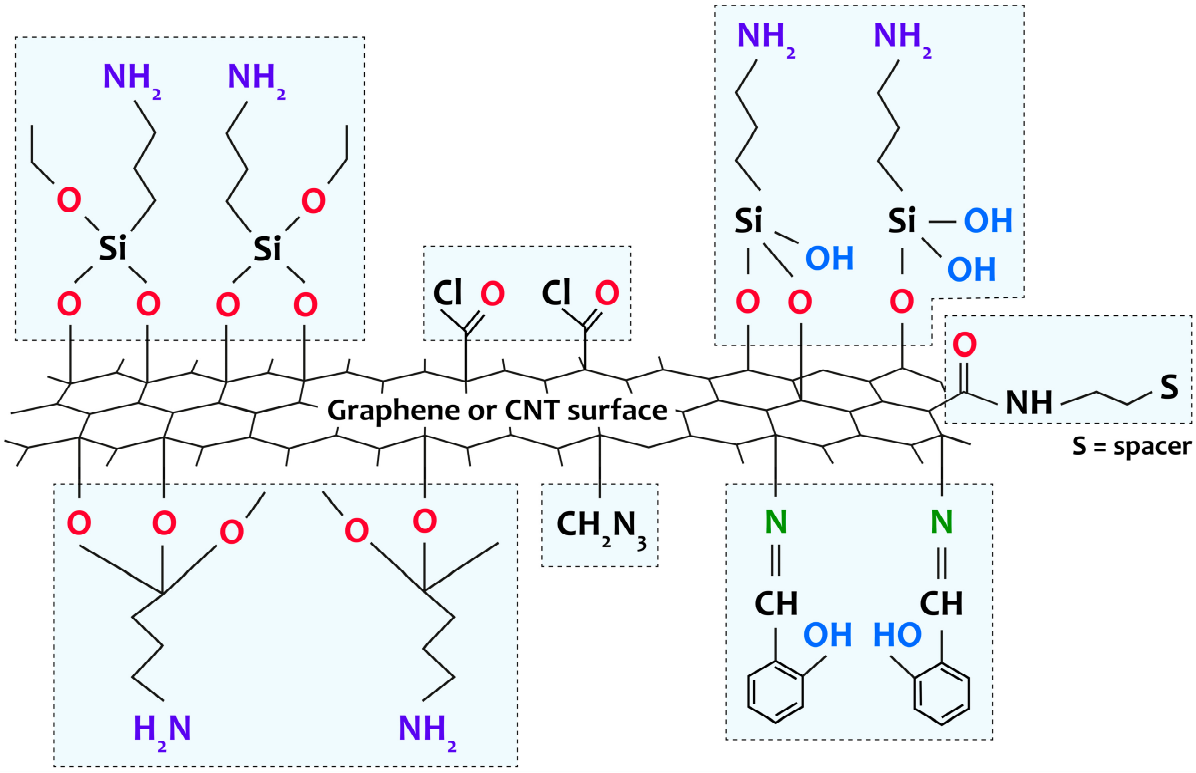

Figure 5. Representation of various groups covalently grafted to the surface of CNTs and graphene by amino-functionalization, chlorination, through spacer attachment, or through direct reaction of the ligand with the surface groups of the carbon support.

For example, the composites [Mn(Salen)]/MWCNTs [100] and [Co(Salen)]/SWCNTs [101] were formed by mixing and reacting both components under ultrasonic conditions without pretreatment of MWCNTs. These composites were then used as a coating for a glass–carbon electrode. In [102,103], a [Ni(Salen)]/MWCNTs composite was prepared by first treating MWCNTs with HNO_3 followed by $SOCl_2$ and then mixing the complex with functionalized MWCNTs in $CHCl_3$ (Figure 6). This material has been used to oxidize primary and secondary alcohols and phenol. In other studies [104,105], [M(Salen)]/MWCNTs (M = Cu, Ni, Co) composites were synthesized via amino-functionalized with 3-aminopropyltriethoxysilane (APTES) or ammonium benzoate. A comparable technique was employed for synthesizing amino-functionalized graphene oxide and preparing [M(Salen)]/GO (M = Mn, Cu, Co, Fe and VO) composites (Figure 6) [106–112]. The preparing composites underwent testing in conditions of catalytic epoxidation of styrene and unfunctionalized olefins as well as lignin oxidation [106–108].

The literature provides several key methods for forming composites of MWCNTs (SWCNTs), graphene, and electrically conductive polymers based on [Ni(Salen)] complexes by electrochemical deposition. One approach is to prepare a conductive electrode with a carbon layer that serves as a substrate for the formation of a polymer, such as poly-[Ni(Salen)] [5,7,42,113,114], poly-[Ni(CH_3-Salen)] [8,114], poly-[Ni(Salphen)] [8,42], poly-[Ni(CH_3-Salphen)] [8], or poly-[Ni(Saldmp)] [42], by using a solution consisting of an electrolyte and a monomer and applying potentiodynamic, conventional, or pulsed

potentiostatic methods. In the studies referred to, it was mainly MWCNTs that were used as the carbon material, with the preparing composites serving as materials for energy storage. However, this method of composite preparation leads to polymer growth primarily on the outer surface of the carbon nanomaterial, which ultimately restricts the access of the electrolyte to a significant portion of the pores. This restriction leads to a decrease in conductivity at the "carbon nanomaterial-metal salen" interfaces, resulting in a deterioration of the electrochemical properties [61]. To overcome this limitation, a technique of carbon nanomaterial presoaking in a metal–salen monomer's highly concentrated solution is utilized to adsorb the complex both on the surface and in the volume of the pores. This technique was first applied to composites of poly-[Ni(Saltmen)]/porous carbon, poly-[Ni(Salen)]/porous carbon, poly-[Ni(3-CH_3O-Salen)]/porous carbon [47,115], and subsequently to composites of poly-[Ni(CH_3-Salen)]/SWCNTs [6] and poly-[Ni(Salen)]/MWCNTs [116]. The prepared material can then be transferred to a low concentration monomer solution or a solution without monomers for electrochemical polymerization. At the adsorption step, the degree of pore filling in the carbon nanomaterial can be regulated. Afterwards, it can be dried for long-term storage without the loss of the monomeric metal–salen component. An alternative method involves codepositing polymer and carbon material from a mixture of a monomer solution in an electrolyte and a suspension of carbon material, followed by the formation of a composite coating on a conductive electrode [58]. Poly-[Ni(Salen)]/MWCNTs [9], poly-[Ni(3-CH_3O-Salen)]/graphene [114], and poly-[Ni(3-CH_3O-Salen)]/N-FLG (nitrogen-doped few-layer graphene) [37] composite films were synthesized using this method. However, this approach has a number of disadvantages associated both with obtaining a uniform dispersion of carbon nanomaterials and with the reproducibility of the structure and, accordingly, the characteristics of the composite.

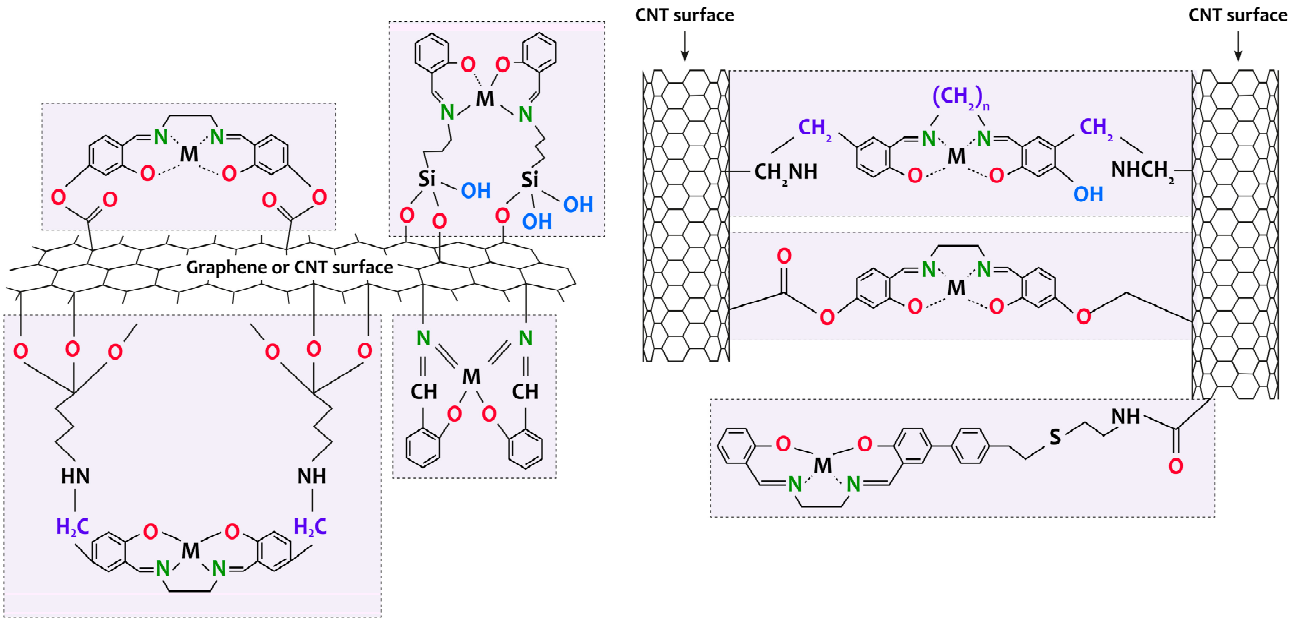

Figure 6. Schematic representation of the formation of [M(Salen)]/carbon nanotubes and [M(Salen)]/graphene composites.

Therefore, to prepare poly-[M(Salen)]/SWCNTs (or MWCNTs) and poly-[M(Salen)]/graphene composites with a uniformly distributed polymer layer on the carbon material surface and pores, as well as high interfacial adhesion at the "polymer-carbon material" interfaces, predeposition of carbon material on the conducting electrode, additional functionalization of the surface of the carbon material, and subsequent soaking in a concentrated monomer solution are required steps. As a result, synergistic effects of the two phases may occur, leading to an improvement in a number of properties of the composite and the creation of new functionality.

3. Local Atomic and Electronic Structure of [M(Salen)] Complexes, Their Polymers, and Composites with Carbon Nanostructures: X-ray Spectroscopic Data

3.1. X-ray Spectroscopic Methods for Diagnosing Atomic and Electronic Structure

This part of the review examines the physical principles and capabilities of the XPS, VB PES, and X-ray absorption spectroscopy (NEXAFS and EXAFS) methods for obtaining information about the local atomic and electronic structure of polyatomic systems.

3.1.1. XPS

XPS is a widely used X-ray spectroscopic method for studying the characteristics of the filled inner (core) electron shells of atoms in solid, adsorbed, and gas-phase polyatomic systems [117–119]. Core-level photoemission spectra are used to measure the binding energy (E_{bin}) of the core electrons of atoms and their energy differences (chemical shifts) in various compounds. This method is based on measuring the kinetic energy of photoelectrons ejected from the inner electron shells of atoms when X-ray photons are absorbed and is schematically shown in Figure 7a. In this case, the photoelectron emission process is described by the following Einstein's equation:

$$h\nu = E_{bin} + E_k + \varphi, \quad (1)$$

where $h\nu$ is the energy of the incident photon, E_{bin} is the binding energy of the core-level electron, E_k is the kinetic energy of the photoelectron emitted as a result of the photoelectric effect, and φ is the work function of the spectrometer material [117]. Since the values of $h\nu$ and φ are known, and E_k is determined experimentally, Equation (1) makes it easy to calculate E_{bin}. Due to the fact that each chemical element has its own set of E_{bin} values for the inner electron shells, the photoelectron spectrum reflects the elemental composition of the substance and chemical states of its atoms. Thus, XPS can be used to obtain information about the concentration of elements by determining the relative total intensities of the corresponding photoelectron lines. An important role when considering XPS spectra is also played by the analysis of changes (chemical shifts) in the binding energies of the inner electron shells of an atom in its various compounds. In this case, very valuable information can be obtained about the chemical state of the atom absorbing the X-ray photon and its change when moving to another compound.

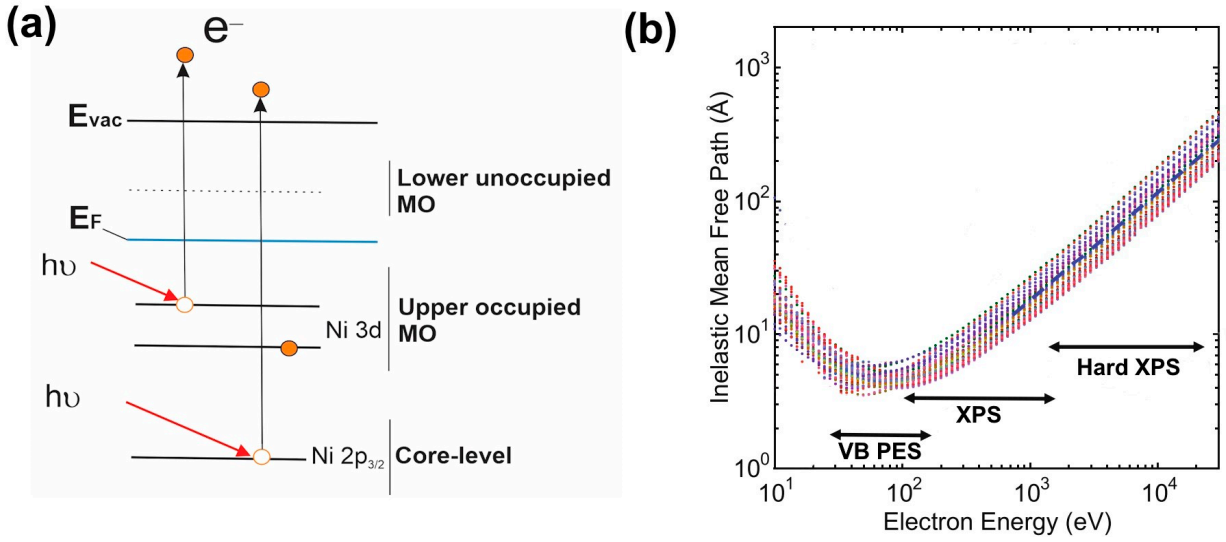

Figure 7. Schematic representation of the photoionization process (core or valence electron) (**a**) and energy dependence of inelastic mean free path λ of photoelectrons calculated for the 41 elements from the often-used formula TPP-2 M (adapted from Ref. [120] with permission) (**b**).

It should be noted that the radiation sources in laboratory XPS spectrometers are the characteristic Mg Kα, Al Kα, Ti Lα, Cu Lα, Ag Lα, and other X-ray lines generated by an X-ray tube with a corresponding anode [117]. Of these, the Mg Kα and Al Kα lines are the most commonly used photon sources due to their narrow full width at half maximum (FWHM) (0.7–0.85 eV). They are also suitable for a wide range of operating binding energies (from the Fermi level to 1240 and 1470 eV, respectively).

The inner electron shells of atoms can be ionized by X-ray photons at a sufficiently large depth relative to the surface of the material. However, not all of the generated photoelectrons leave the sample, and most of them are lost on the way to the surface due to various processes of their scattering. Ultimately, only photoelectrons from a thin near-surface layer can be detected, determined by the mean free path (λ) of the photoelectron in the material under study. As can be seen from Figure 7b, in the range of kinetic energies characteristic of XPS (<1500 eV), the electron mean free path is limited to several nanometers (about 1–5 nm), and in the energy range 50–200 eV, less than 1 nm. It should be noted that approximately 65% of the signal intensity is formed due to photoelectrons emitted from the surface layer with a thickness of less than λ, 85% with a thickness of less than 2λ, and 95% with a thickness of less than 3λ. Thus, this method is surface-sensitive.

A more advanced source of X-ray radiation is synchrotron radiation from modern electron storage rings. These radiation sources are characterized by a unique set of properties, namely, a wide continuous spectrum of X-ray radiation with photon energies ranging from several tens of electronvolts to several tens of kiloelectronvolts, high intensity, and a significant degree of polarization in the electron orbital plane, as well as the temporal structure of the X-ray beam. Recently, there has been increased interest in XPS studies using high-energy synchrotron radiation photons with energies in the range of 5–15 keV, the so-called hard XPS. Here, it is possible to increase the escape depth of XPS analysis from 1–5 to 10–15 nm (see Figure 7b) and, more importantly, obtain additional structural data based on the effects of high-energy photoelectron diffraction [119]. Processing of XPS spectra is carried out using specialized software, for example, CasaXPS ver. 2.3.25 [121], Thermo Avantage ver. 5.9931, or XPSPEAK ver. 4.1, by analyzing survey spectra (determination of chemical composition) or individual photoelectron lines (chemical analysis).

3.1.2. VB PES

The main method for obtaining information about the energy distribution of occupied electron states in the valence band of a polyatomic system is valence-band photoemission spectroscopy (VB PES), which uses ultraviolet radiation (He(I) and He(II) resonance lines of gas-discharge sources with photon energies $h\nu$ of 21.2 and 40.8 eV, respectively) and synchrotron radiation in the soft X-ray range with photon energies $h\nu$ of 50–150 eV to excite photoemission spectra from the valence band (Figure 7a) [117]. The valence-band electronic structure of a polyatomic compound is characterized by the energy distribution of the density of states (DOS) for occupied electron states, which in turn are described by combinations of valence atomic orbitals (AOs) of all atoms of the compound. The different dependences of the photoionization cross sections on the energy of exciting photons for valence AOs of different atoms [122] cause noticeable differences in the shape of the experimental VB PE spectrum from the calculated energy dependence of DOS for occupied valence states. When the energy of the exciting photons changes, the intensity of the main PE bands usually changes significantly, which is clearly observed in Figure 8. Thus, by considering the behavior of the intensity of VB PE bands with changes in the energy of exciting photons, it is possible to obtain certain information about the origin of these bands in the valence band of a polyatomic system and their relationship to the partial DOS of individual atoms. In this regard, it is advisable to study VB PE spectra, exciting them with photons with energies in a wide energy range encompassing both ultraviolet and soft X-ray radiation.

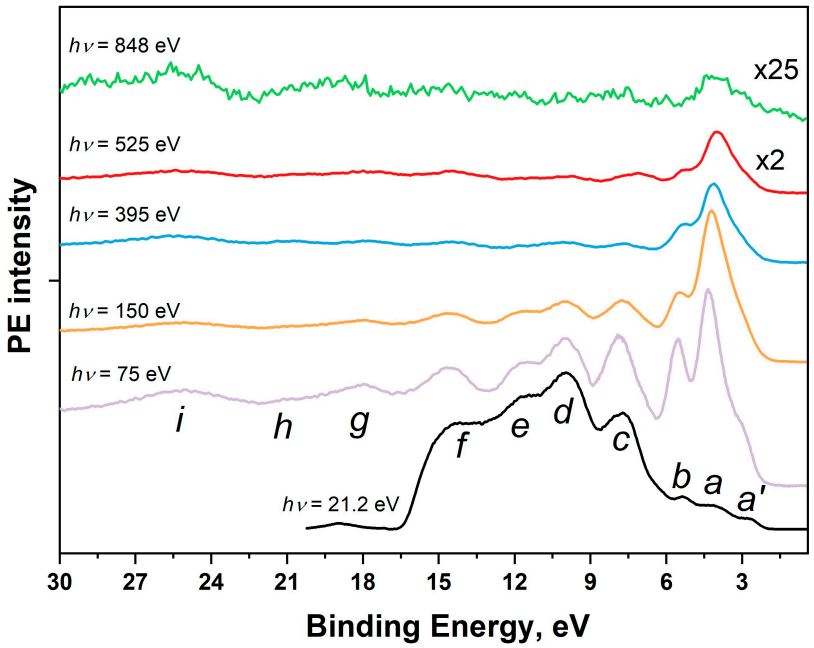

Figure 8. VB PE spectra of the [Ni(Salen)] complex excited by photons with energies $h\nu$ from 21.2 eV to 848 eV. The lowercase letters a', a, b, c, d, e, f, g, h and i denote the photoemission signals of individual sub-bands of the valence band [53].

Additional information about the electronic structure of the valence band can also be obtained using the method of resonance photoemission (ResPES), which is especially useful in the study of compounds of transition and rare earth metals, in particular, 3*d* metals [123–125]. This method is implemented by measuring VB PE spectra at photon energies of localized core-excited states (absorption resonances) in the NEXAFS spectrum of metal atoms of the polyatomic system under study. When the VB PE spectra of [Ni(Salen)] are excited by photons with energies in the region of the Ni $2p_{3/2} \rightarrow 3d$ absorption resonance, distinct changes in the structure of the spectra are observed, namely, a strong increase in the intensity of some PE bands in the low E_{bin} region and the appearance of additional, very intense bands at high E_{bin} (Figure 9). The increase in intensity occurs due to the superposition of two processes. The first one is associated with the direct photoionization of occupied Ni 3*d*-derivated MOs in the valence band of [Ni(Salen)] ($2p^6 3d^8 + h\nu \rightarrow 2p^6 3d^7$ + e), while the second process is due to the participator-Auger (*pA*) decay of the Ni $2p^5 3d^9$ core (resonance) excitation ($2p^6 3d^8 + h\nu \rightarrow 2p^5 3d^9 \rightarrow 2p^6 3d^7$ + e), the final state of which coincides with that of direct photoionization (Figure 10). In turn, the appearance of additional bands in the VB PE spectra is caused by the spectator-Auger (*sA*) decay of the Ni $2p^5 3d^9$ resonance excitation. All of the above processes are shown schematically in Figure 10 and are clearly visible in Figure 9 when considering the VB PE spectra of the [Ni(Salen)] complex excited at a photon energy of 854.4 eV (corresponding to the value of maximum *A* of the most intense resonance in the Ni $2p_{3/2}$ NEXAFS spectrum). When considering Figure 9, it is important to emphasize that after the energy of the exciting photons passes through resonance *A*, the intensities of the *pA*, sA_1, and sA_2 bands gradually decrease, and at photon energies above 859 eV, the VB PE spectrum practically returns to its initial shape. Thus, the analysis of resonance VB PE spectra makes it possible to determine the energy localization in the valence band of [Ni(Salen)] of occupied electronic states with the Ni 3*d* contributions. Obviously, this experimental technique can be informative for the examination of the electronic structure of the valence band of complexes [M(Salen)] with other 3*d* atoms.

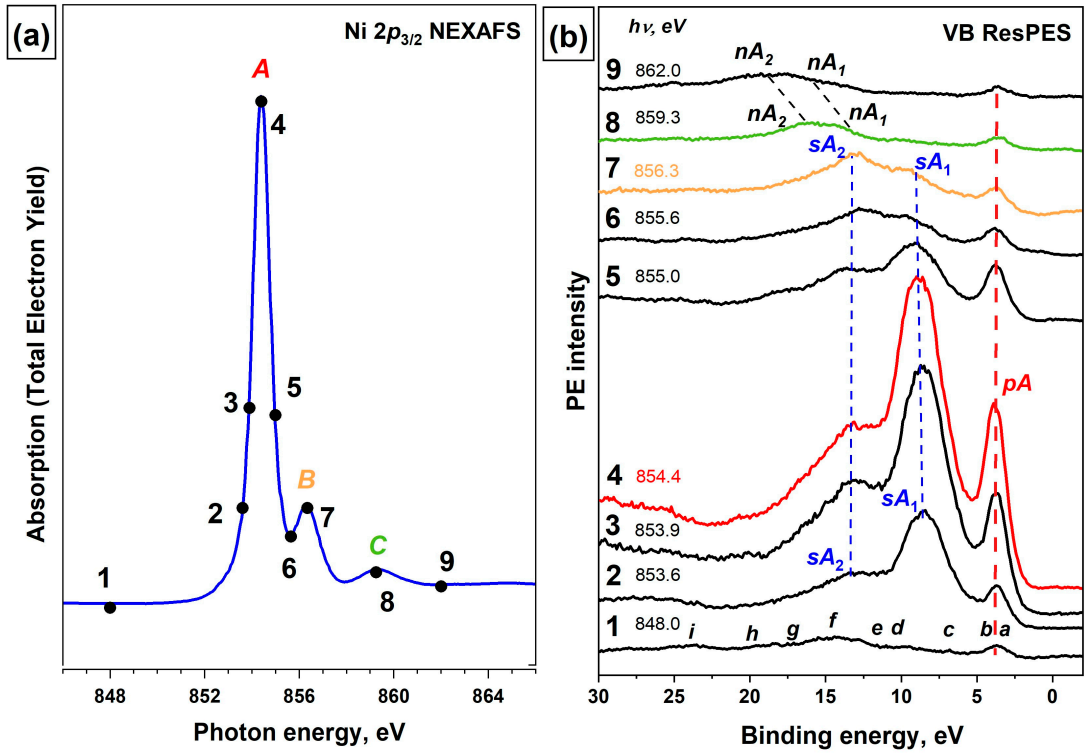

Figure 9. (**a**) Ni $2p_{3/2}$ NEXAFS spectrum of [Ni(Salen)]; the photon energies used to excite the VB PE spectra are marked with numbered dots. (**b**) A series of resonant VB PE spectra of [Ni(Salen)]. *pA*—electron band due to participator-Auger decay; sA_1 and sA_2—low- and high-energy electron bands due to spectator-Auger decay; nA_1 and nA_2—electron bands due to normal Auger decay of Ni $2p_{3/2}{}^{-1}3d^9$ excitations. The lowercase letters *a*, *b*, *c*, *d*, *e*, *f*, *g*, *h* and *i* denote the photoemission signals of individual sub-bands of the valence band [53].

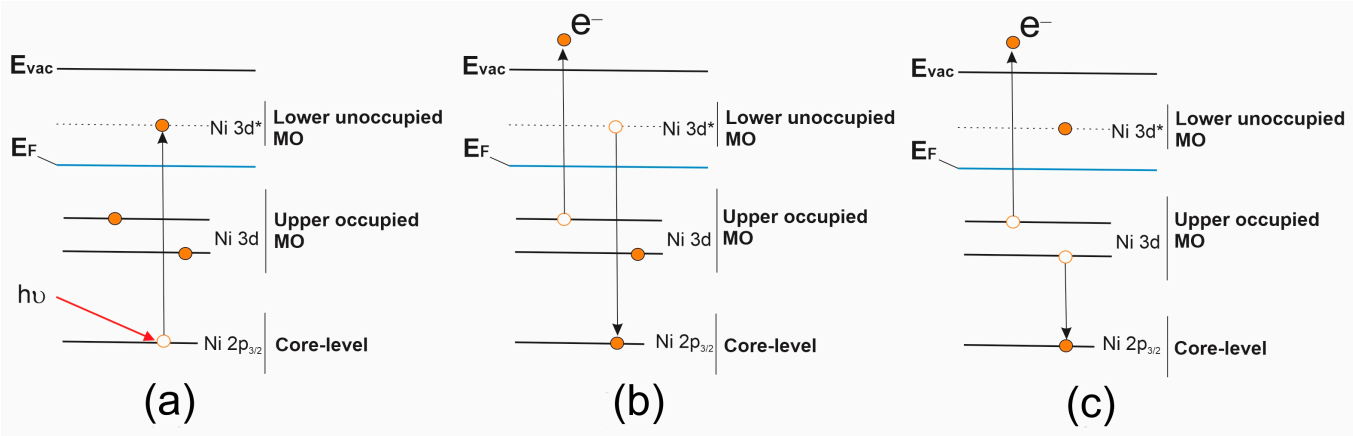

Figure 10. Schematic representation for resonant core electron excitation process (**a**) and Auger electron decay processes of a resonant excitation: (**b**) participator-Auger (*pA*) electron decay and (**c**) spectator-Auger (*sA*) electron decay [53].

3.1.3. NEXAFS and EXAFS

X-ray absorption spectroscopy is currently one of the most powerful experimental methods for obtaining information about the local atomic and electronic structure of polyatomic systems. Within the framework of this technique, two spectroscopic methods are usually distinguished, namely, near-edge X-ray absorption fine structure (NEXAFS) and extended X-ray absorption fine structure (EXAFS) spectroscopy, differing in their origin, methods of obtaining spectra, and analysis. NEXAFS spectroscopy is used to

obtain information about low-lying unoccupied electronic states in a polyatomic system and is based on the analysis of absorption bands in the immediate vicinity of the X-ray absorption edge—about 10 eV below and 30 eV above the absorption edge (Figure 11a). It is conventional to describe these spectra using multiple (resonant) scattering of photoelectrons ejected from the core of an absorbing atom on the nearest neighbor atoms [126,127]. At certain photoelectron energies, a quasi-molecule formed by neighborhood atoms can temporarily trap a photoelectron, resulting in the formation of metastable states (shape resonances). These resonances, depending on their lifetime, are observed in the spectrum as narrow lines or broad absorption bands. Resonance localization in the quasi-molecule field allows us to consider them as a result of dipole-allowed transitions of core electrons to the unoccupied MOs of this polyatomic system.

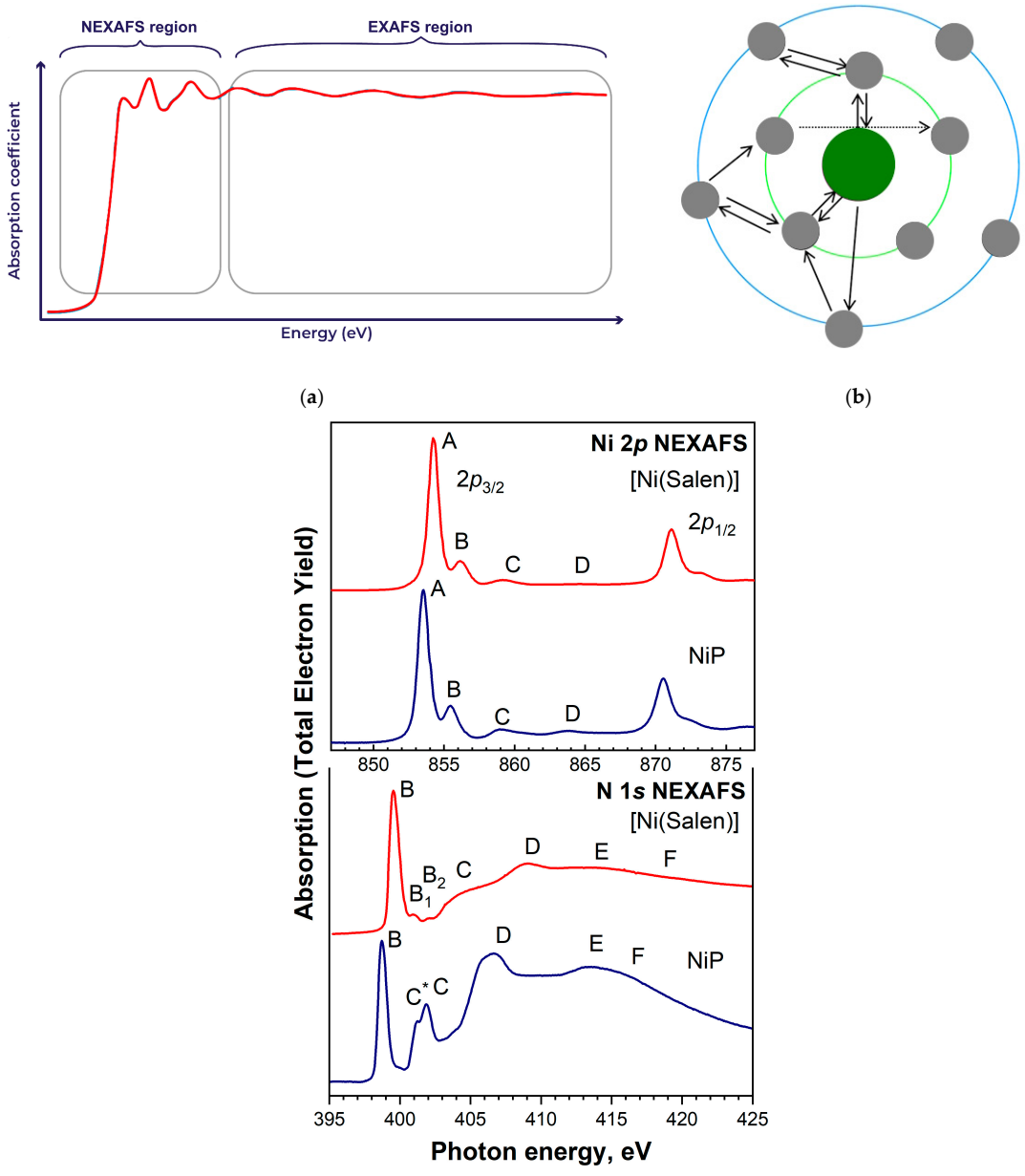

Figure 11. (**a**) X-ray absorption spectrum with regions corresponding to NEXAFS and EXAFS, and (**b**) schematic representation of NEXAFS mechanism due to multiple scattering. (**c**) Ni $2p_{3/2,1/2}$ and N 1*s* NEXAFS spectra of [Ni(Salen)] compared to the corresponding spectra of nickel porphyrin NiP [45].

It should be emphasized that the dominant role of the processes of multiple scattering of photoelectrons in the NEXAFS region is due to their low kinetic energy, which leads to large photoelectron wavelengths, which turn out to be comparable to the interatomic distances between the absorbing atom and its neighboring atoms (Figure 11b). As the kinetic energy of photoelectrons increases (>50 eV), their wavelength quickly decreases and the processes of multiple scattering of photoelectrons become unlikely.

The promise of using the above quasi-molecular approach in the analysis of NEXAFS spectra is demonstrated by a direct comparison of the corresponding spectra of the nickel salen [Ni(Salen)] and nickel porphyrin NiP complexes in Figure 11c. Both complexes have similar square–planar coordination centers (quasi-molecules) [NiN_2O_2] and [NiN_4] with close interatomic distances. Despite the general similarity of the spectral behavior of the corresponding Ni 2*p* and N 1*s* NEXAFS spectra of the complexes, the compared spectra demonstrate noticeable differences in the fine structure (energy shifts of absorption bands, changes in their intensities, the appearance of additional bands, etc.), which are logically associated with a change in the coordination center when moving from salen to the porphyrin complex. Thus, NEXAFS spectroscopy is one of the most informative methods for studying polyatomic systems due to its sensitivity to the ordering, binding energy, atomic orbital composition, and angular symmetry of empty MOs; bond lengths and angles; nearest neighborhood coordination, etc. [55,59].

Studies of EXAFS spectra with the energy region of EXAFS oscillations from 30 to ~1500 eV above the absorption edge allows one to determine with sufficiently high accuracy distances and coordination numbers around a specific absorbing atom, thus providing probing of the local atomic structure of a polyatomic system near the absorbing atom (Figure 11a) [128]. At present, it can be considered clear that the main features of the EXAFS structure are caused by the processes of elastic scattering of a photoelectron wave by the potential relief of the nearest neighborhood of the absorbing atom in a polyatomic system [129,130]. This primary wave is scattered by neighboring atoms through acts of single backscattering of electrons and generates scattered waves that can interfere (constructively or destructively) with the primary wave (see Figure 12), which leads to the appearance of EXAFS oscillations [129]. In this case, the amplitude of the scattered electron wave is equal to the sum of contributions from each of the surrounding atoms [131]. To describe this process, it is necessary to determine the normalized EXAFS function $\chi(k)$, which contains all the information about the oscillations of the photoionization cross sections of atoms in the substance. This function can be found through Equation (2):

$$\chi(k) = \sum_j \frac{N_j \cdot f_j(k) \cdot e^{-2k^2 \cdot \sigma_j^2}}{k \cdot R_j^2} \cdot \sin\left[2k \cdot R_j + \delta_j(k)\right] \quad (2)$$

where k is the wave number of the photoelectron wave, $f_j(k)$ is the amplitude of the backscattered electron wave by atoms of the coordination sphere, $\delta_j(k)$ are phase shifts, N_j is the number of neighboring atoms to atom j, R_j is the distance to atom j, and ${\sigma_j}^2$ is the Debye–Waller factor, characterizing the root mean square amplitude of the deviation of the distance to atoms of type j from the average value caused by structural and thermal disorder [130].

In order to separate the contributions of individual coordination spheres from the overall function $\chi(k)$, spectral analysis methods are used by expansion of the function $\chi(k)$ into a Fourier integral (see Figure 13). Finally, a Fourier transform is performed into R-space, giving information about the interatomic distances between the absorbing atom and nearby atoms (see Figure 13d). In view of the above, EXAFS spectroscopy is most often used to obtain primary structural information about new chemical compounds (chemical bond lengths, coordination numbers, and type of atoms surrounding the studied one) within the range of 4–5 Å (the first few coordination spheres). In this case, EXAFS spectroscopy is usually implemented for the 1*s* and 2*p* shells of elements with a charge number Z > 20 [128,130].

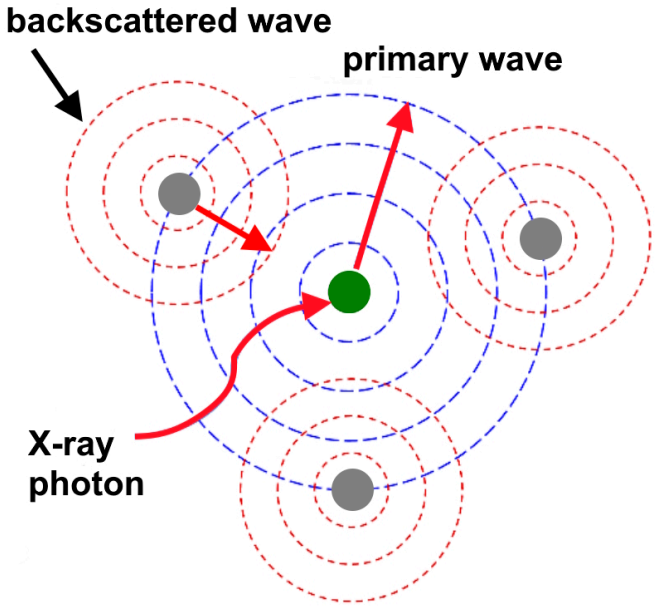

Figure 12. Schematic view of the formation mechanism of EXAFS oscillations [131].

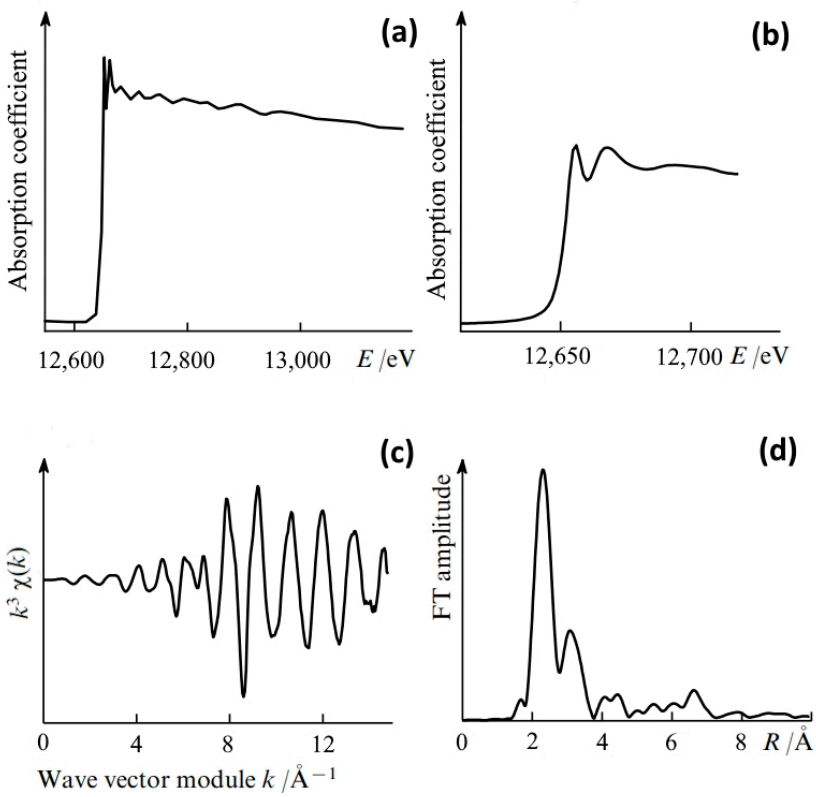

Figure 13. Steps of EXAFS data processing: (**a**) an experimental X-ray absorption spectrum; (**b**) the amplified NEXAFS region; (**c**) the normalized EXAFS curve (the oscillating part of the X-ray absorption coefficient); and (**d**) the Fourier transform (FT) of the normalized EXAFS curve; the maxima of the Fourier transform correspond to the coordination spheres around the central atom [129].

It is important to note that X-ray absorption (NEXAFS, EXAFS) spectra can be measured in various modes such as transmission and fluorescence as well as total electron and Auger electron yield modes. More detailed information about each of these methods is given in [126,128,132]. At the same time, to measure the ones being studied, most researchers use synchrotron radiation beamlines at electron storage rings. EXAFS data

processing is usually carried out using the Athena and Artemis programs, which are part of IFEFFIT [133]. These programs include AUTOBK for background removal, FEFF6L for creating theoretical EXAFS models, and FEFFIT for optimizing model parameters. Figure 13 presents the main stages of processing EXAFS oscillations.

3.2. Atomic and Electronic Structure of [M(Salen)] Complexes and Their Polymers

3.2.1. XPS

Research in recent years has been characterized by individual attempts to use the XPS method to obtain information on the chemical state of functional atoms in monomers and their poly-[M(Salen)] polymers, as well as on the atomic structure of these polyatomic systems [26,39,43–46,48–52,114]. It should be noted that all the cited measurements of XPS spectra are mainly of a test nature, and most of them were performed on laboratory installations using X-ray tubes as radiation sources with low energy resolution and insufficiently good statistics. For monomers, there are only a few works [39,44–46,50–52] in which the positions of binding energies of the 1s electrons of the ligand atoms (N, C, O) as well as 2*p*, 3*d*, or 4*f* electrons of the corresponding metal atoms were measured for the complexes [M(Salen)] (M = Cu, Ni, Co, Pd, Pt) using the XPS method (Table 2). From the data in Table 2, the trends in the shifts of the O 1*s* lines (to lower binding energies) and N 1*s* lines (to higher binding energies) in going from a molecule (salen without a metal) to complexes are clearly visible, which indicates a redistribution of the valence electron density between the metal and ligand atoms. However, all these measurements, with the exception of those in works [45,46], were carried out mainly on powdered samples that can be charged as a result of X-ray irradiation, thereby distorting the real binding energies of core electrons. To eliminate charging, the H_2(Salen) and [Ni(Salen)] samples for XPS measurements were prepared *in situ* in the form of thin (about 10–50 nm thick) layers using thermal evaporation of dehydrated powders of the corresponding substances from a quartz crucible and subsequent deposition onto clean polycrystalline platinum plates under ultrahigh vacuum conditions (about 10^{-9} mbar). Herewith, Ni 2*p*, O 1*s*, N 1*s*, C 1*s* photoelectron spectra for the systems under study were measured using monochromatic Al Kα radiation ($h\nu$ = 1486.6 eV) with an analyzer pass energy of 10 eV and good statistics (more than 10^3 counts at each point).

Table 2. Binding energies (E_{bin}) of the 1*s*, 2*p*, 3*d*, and 4*f* electrons of the corresponding atoms measured by XPS for H_2(Salen), [Cu(Salen)], [Ni(Salen)], [Pd(Salen)], [Pt(Salen)], and [Co(Salen)] and some polymers based on them.

Compound	E_{bin}, eV				Calibration	Ref.
	C 1*s*	N 1*s*	O 1*s*	M 2*p*, 3*d*, 4*f*		
H_2(Salen)	285.0 285.5 286.5	399.0 ± 0.1	532.9 ± 0.1	-	C 1*s* 285.0 eV	[39]
[Cu(Salen)]	285.0 286.6	399.5 ± 0.1	531.3 ± 0.1	Cu $2p_{3/2}$ 936.4		
[Ni(Salen)]	285.0 286.15	399.6 ± 0.1	531.3 ± 0.1	Ni $2p_{3/2}$ 855.2		
[Pd(Salen)]	285.0 285.9 286.6	399.9 ± 0.1	531.4 ± 0.1	Pd $3d_{5/2}$ 338.5		
[Pt(Salen)]	285.0 286.4	400.1 ± 0.1	531.6 ± 0.1	Pt $4f_{7/2}$ 73.4		
H_2(Salen)	not specified	398.4	not specified	-	C 1*s* 285.0 eV	[52]
[Co(Salen)]	not specified	399.0	not specified	Co $2p_{3/2}$ 780.4		
H_2(Salen)	not specified	398.3 ± 0.1	532.2 ± 0.1	-	Au $4f_{7/2}$ 83.4 eV	[51]
[Cu(Salen)]	not specified	389.9 ± 0.1	530.8± 0.1	Cu $2p_{3/2}$ 934.5 ± 0.1		
[Ni(Salen)]	not specified	399.4 ± 0.1	531.2± 0.1	Ni $2p_{3/2}$ 855.0 ± 0.2		
[Co(Salen)]	not specified	398.9 ± 0.2	530.9 ± 0.2	Co $2p_{3/2}$ 779.9 ± 0.1		[50]

Table 2. *Cont.*

Compound	E_{bin}, eV				Calibration	Ref.
	C 1*s*	N 1*s*	O 1*s*	M 2*p*, 3*d*, 4*f*		
H_2(Salen)	284.8 286.2	398.65	532.5	-	Pt $4f_{7/2}$ 71.1 eV	[46]
[Ni(Salen)]	285.75 287.25	400.55	532.1	no information		
[Ni(Salen)]	285.5 287.0	400.3	532.0	Ni $2p_{3/2}$ 856.3	Pt $4f_{7/2}$ 71.1 eV	[45]
[Ni(Salen)]	not specified	398.4	530.2	Ni $2p_{3/2}$ 854.3	C 1*s* 284.8 eV	[44]
poly-[Ni(Salen)]	not specified	399.1	530.2	Ni $2p_{3/2}$ 854.9	C 1*s* 284.8 eV	[44]
poly-[Ni(CH_3O-Salen)] ox	not specified	399.8	531.5, 533.3, 534.6	Ni $2p_{3/2}$ 854.9	C 1*s* 284.8 eV	[48]
poly-[Ni(CH_3O-Salen)] red	not specified	399.8	531.5, 533.3, 534.6	Ni $2p_{3/2}$ 854.9		
poly-[Cu(Salen)] ox	not specified	399.5 ± 0.1	531.2 ± 0.1	not specified	C 1*s* 285.0 eV	[39]
poly-[Cu(Salen)] red		399.4 ± 0.1	531.2 ± 0.1			
poly-[Ni(Salen)] ox		399.7 ± 0.1	531.3 ± 0.1			
poly-[Ni(Salen)] red		399.6 ± 0.1	531.2 ± 0.1			
poly-[Pd(Salen)] ox		399.8 ± 0.1	531.3 ± 0.1			
poly-[Pd(Salen)] red		399.8 ± 0.1	531.2 ± 0.1			
poly-[Pt(Salen)] ox		400.4 ± 0.1	532.4 ± 0.1			
poly-[Pt(Salen)] red		400.3 ± 0.1	531.9 ± 0.1			
[Pd(3-CH_3Salen)]	285.0 286.4 291.1	400.0	531.6	Pd $3d_{5/2}$ 338.7	C 1*s* 285.0 eV	[40]
poly-[Pd(3-CH_3Salen)] ox	284.2 285.6 287.2 289.1	399.2 401.3 403.1	531.7	Pd $3d_{5/2}$ 337.9		
poly-[Pd(3-CH_3Salen)] red	284.6 285.9 287.1 289.6	399.6 402.9	531.3	Pd $3d_{5/2}$ 338.2		

The important results obtained in these works include that the carbon atoms in the complex form two groups of atoms, Cα (C1, C4) and Cβ (C2, C3, C5), with similar chemical (charge) states, which are associated with carbon atoms in phenyl rings or with nitrogen and oxygen atoms in phenolic and ethylenediamine fragments, respectively (see Figure 1). It was found that the observed shifts of C 1*s* (+1.0 eV), N 1*s* (+1.9 eV), and O 1*s* (−0.4 eV) photoelectron lines in going from H_2(Salen) to [Ni(Salen)] are caused by the chemical bonding of the Ni 3*d* atom with salen ligand atoms and, as a result, a redistribution of valence electron density between the metal and ligand atoms (see Figure 14). It is also noted that the different signs of the chemical shifts indicate that the transfer of electron density to the O atoms in [Ni(Salen)] occurs not only from the Ni atom but also from the N and C atoms.

In the case of polymers, the most interesting of the studies mentioned above are the works [26,39], in which the XPS method, along with testing the purity and stoichiometry of polymers, was first used to study the distribution of the valence electron density and changes in the binding energies of inner-shell electrons in a large number of electro- and photoactive polymers poly-[M(Salen)] with M = Cu(II), Ni(II), Pd(II), Pt(II). Based on a comparative analysis of the binding energies of the inner 1s electrons of functional nitrogen and oxygen atoms, it was found that the binding energies of these electrons do not change significantly in going from monomer to polymer, thus indicating the stability of the coordination center in the monomer during the process of electrochemical polymerization (see Table 2). It was also established that the formation of the [M(Salen)] complexes is accompanied by the appearance of an excess electron density on oxygen ions, which,

apparently, is then used in the electrically stimulated oxidation of the monomeric complex. In this regard, it was suggested that the electronic state of oxygen in the salen ligand plays a key role in the formation of the polymer structure. In other words, during the oxidation of the monomer at the anode, the oxygen ions of the coordination center perform the function of an electronic "depot", being a source of electrons during the electrochemical oxidation of each structural unit. Among the important results obtained in these works, one should also include the observation that after XPS measurements, polymer samples retained their electrically conductive and optical properties, i.e., they were not destroyed or transformed in a noticeable way during their irradiation with intense beams of ionizing X-rays. All this additionally indicates the promise of using X-ray spectroscopy methods to study the properties of electrically conductive polymers.

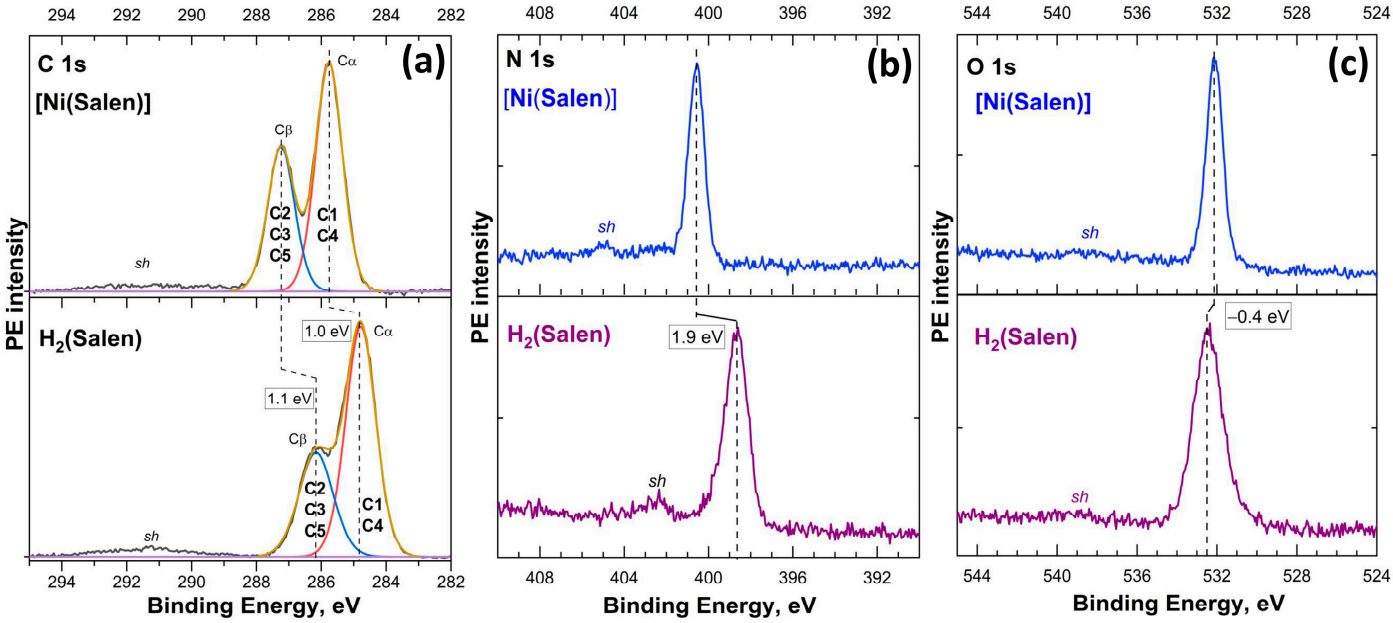

Figure 14. C 1*s* (**a**), N 1*s* (**b**), and O 1*s* (**c**) photoelectron spectra of the H_2(Salen) molecule and [Ni(Salen)] complex measured using Al Kα radiation ($h\nu$ = 1486.6 eV) and plotted on the scale of electron binding energies relative to the Fermi level [46].

To summarize, it is important to say that the XPS method is effective for studying the change in the binding energy of core electrons of ligand atoms (C, N, O) and complexing metal atoms in going from monomer fragments to polymers. In other words, its use allows one to obtain important information about the chemical (charge) state of all atoms of such a polyatomic system. However, as follows from this literature review, only a few works contain detailed information about the binding energies for the inner-shell electrons of atoms.

3.2.2. VB PES

As noted above in this review, studies of occupied electronic states of the valence band for monomers [M(Salen)] and their polymers using valence photoemission (VB PE) have so far been limited to a few works [45,46,53]. These works are devoted to studying the electronic structure of only the H_2(Salen) molecule and the [Ni(Salen)] complex. These VB PE spectra were recorded with high energy resolution using exciting photon energies of 21.2 eV (He(I) resonance source) and 75, 150 eV (synchrotron radiation) from thin layers of the corresponding substances deposited *in situ* by thermal evaporation on clean Pt plates under ultrahigh vacuum conditions (about 10^{-9} mbar). DFT calculations were additionally used to interpret the VB PE spectra [45,46]. Important results obtained in these works are that the photoelectron bands observed in the valence-band spectra in the binding energy

range of 8–17 eV are mainly associated with σ molecular orbitals, in which contributions from the C 2*s* and C 2*p* AOs predominate. In turn, in the low-energy region of 2–6 eV there are bands associated with molecular orbitals with dominant contributions from Ni 3*d* AOs. In addition, DFT calculations of total and partial DOS for the valence band of both compounds were found to well describe the shape of their experimental VB PE spectra. In the case of [Ni(Salen)] compared to H_2(Salen), the center of gravity of partial N 2*p* and C 2*p* DOS is shifted toward higher binding energies, while that of O 2*p* DOS is shifted in the opposite direction (Figure 15). This finding is explained by an increase in the effective charges of carbon and nitrogen atoms and a corresponding decrease in the effective charge of oxygen atoms in the ligand during the formation of the [Ni(Salen)] complex. An equally interesting result was obtained in the work [53], where VB PE spectra of the molecular complex [Ni(Salen)] were measured using ultraviolet, soft X-ray, and resonance photoemission methods using photons with energies from 21.2 to 848 eV. As a result, it was established that electronic states at a binding energy of 3.8 eV are associated specifically with the Ni 3*d*-derived MOs of the complex (see Figure 8). More detailed information is provided in Section 3.1.2 of the current review.

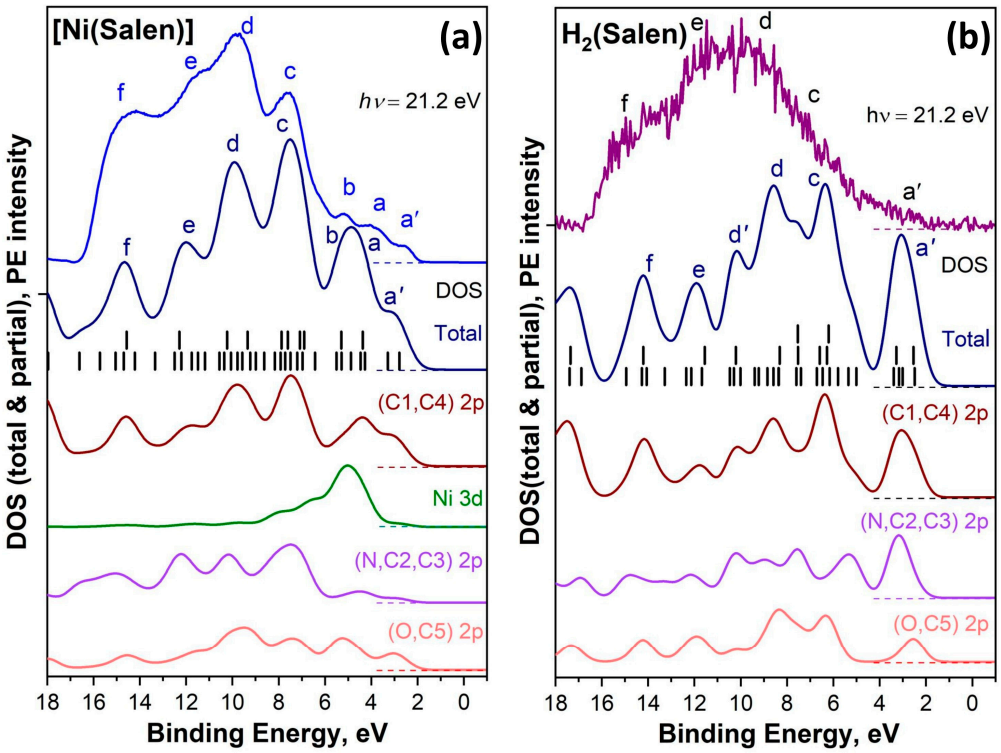

Figure 15. Comparison between experimental valence band and DOS spectra that were from DFT calculations for [Ni(Salen)] complex (**a**) and H_2(Salen) (**b**). Vertical black bars show the energy positions of valence molecular orbitals, which have been broadened by Gaussian lines with a full width at a half maximum of 1 eV. The lowercase letters *a*′, *a*, *b*, *c*, *d*, *e* and *f* denote the photoemission signals of individual sub-bands of the valence band [46].

Thus, a combined experimental and theoretical approach to studying the occupied electronic states of the valence band can be successfully used for other metal–salen complexes. At the same time, it should be emphasized that for poly-[M(Salen)] polymers, studies of occupied electronic states of the valence band using valence photoemission are currently completely absent.

3.2.3. NEXAFS and EXAFS

The application of X-ray absorption spectroscopy (NEXAFS and EXAFS) methods for the characterization of [M(Salen)] monomers and their polymers has so far also been limited

to just a few works [27,29,30,40,45,46,52–56], in which X-ray absorption spectra of metal atoms were used to test the purity and stoichiometry of the sample (Ni 1*s* NEXAFS [27], Ni 2*p* NEXAFS [29], Cu 1*s* NEXAFS [54], Co 1*s* NEXAFS [52,55]) or characterization of the atomic coordination of a metal atom in a polymer (Ni 1*s* EXAFS, Ba 1*s* EXAFS [27,30], Pd 1*s* EXAFS [40]). It should also be emphasized that the measured 1*s* NEXAFS spectra of Ni, Cu, Co, and Pd were not analyzed to obtain information about the electronic structure of the studied [M(Salen)] monomers and their polymers. In turn, the EXAFS spectra were used primarily to obtain structural information about the first coordination sphere corresponding to the coordination centers [MO_2N_2] and approximately the next two coordination spheres covering most of the monomer molecule. All these data are summarized in Table 3. In analyzing these data, one can notice that for all complexes, the square–planar geometry of the coordination center is preserved because the values of the M-N and M-O bond lengths are quite close. At the same time, the minimum values of the M-O, M-N bond lengths in the coordination center is observed in the case of the [Ni(Salen)]-type complex with the complexing nickel atom and the maximum value for the [Pd(Salen)] type with the palladium atom.

Table 3. Structural information obtained from the analysis of M 1*s* EXAFS spectra for monomers and their polymers.

Compound	Atomic Pair	N [a]	R [b], Å	Ref.
[Cu(Salen)]	Cu–O2	1	1.86 ± 0.04	[54]
	Cu–O1	1	1.90 ± 0.04	
	Cu–N2	1	1.95 ± 0.002	
	Cu–N1	1	1.95 ± 0.002	
	Cu–Cu	1	3.22 ± 0.03	
[Co(Salen)]	Co–O_s [c]	2.0	1.91 ± 0.02	[55]
	Co–O_l [d]	1.1	2.20 ± 0.02	
	Co–N	2.1	1.83 ± 0.02	
	Co–Co	0.5	2.92 ± 0.02	
[Co(Salen)] nanoparticles	Co–O_s	1.8	1.90 ± 0.02	
	Co–O_l	1.1	2.20 ± 0.02	
	Co–N	1.5	1.81 ± 0.02	
	Co–Co	0.5	2.92 ± 0.02	
[Co(Salen)]	Co–N	2.0	1.90	[52]
	Co–O	2.0	1.86	
[Co(Salen)] in montmorillonite clay	Co–N	2.0	1.90	
	Co–O	2.0	1.86	
	Co–O	1.6	1.99	
[Ni(3-CH_3saltMe)] in powder	Ni–N(O)	3.5	1.83 ± 0.02	[27]
	Ni–C	4.2	2.82 ± 0.02	
	Ni–C	2.2	3.20 ± 0.02	
[Ni(3-CH_3saltMe)] in CH_3CN solution	Ni–N(O)	3.2	1.83 ± 0.02	
	Ni–C	4.7	2.82 ± 0.02	
	Ni–C	2.2	3.20 ± 0.02	
poly-[Ni(3-CH_3saltMe)] ox	Ni–N(O)	3.8	1.84 ± 0.02	
	Ni–C	4.3	2.82 ± 0.02	
	Ni–C	1.5	3.21 ± 0.02	
poly-[Ni(3-CH_3saltMe)] red	Ni–N(O)	3.8	1.84 ± 0.02	
	Ni–C	4.5	2.81 ± 0.02	
	Ni–C	2.0	3.19 ± 0.02	
[Pd(3-CH_3Salen)] powder	Pd–O(N)	4	1.97 ± 0.002	[40]
	Pd–C	6	3.00 ± 0.006	
	Pd–C	2	3.24 ± 0.004	
poly-[Pd(3-CH_3Salen)] ox	Pd–O(N)	4	1.98 ± 0.002	
	Pd–C	6	3.00 ± 0.008	
	Pd–C	2	3.28 ± 0.009	
poly-[Pd(3-CH_3Salen)] red	Pd–O(N)	4	1.97 ± 0.002	
	Pd–C	6	3.0 ± 0.007	
	Pd–C	2	3.24 ± 0.005	

[a]—coordination number. [b]—distance between absorber and backscattered atoms. [c]—short-distance oxygen atom. [d]—long-distance oxygen atom.

The interesting results were also obtained for the monomeric complexes [Cu(Salen)] and [Co(Salen)] in the works [54,55], where it was found that in powder crystals, these complexes are in the form of dimers with d-d stacking having a certain order. No less interesting results were obtained in the studies [27,40] where EXAFS data are presented for [Pd(3-CH_3Salen)], [Ni(3-CH_3saltMe)] monomers, and their polymers in various charge states (reduced and completely oxidized). The authors found that the formal oxidation state of metals in the complexes is +2 and does not change during polymerization or surface immobilization. In addition, it was shown that the geometry of the coordination center remains practically unchanged as a result of polymerization and the redox cycle of the film, indicating that both processes are based on a ligand mechanism.

It should be noted that the 1*s* NEXAFS spectra of functional atoms of nitrogen, oxygen, and carbon in monomers [M(Salen)] and their polymers are known only for the free salen ligand of the H_2(Salen) molecule and the monomer [Ni(Salen)] complex [45,46,53]. The most valuable result obtained is the general similarity of the N 1*s* and C 1*s* NEXAFS spectra of the H_2(Salen) molecule and the [Ni(Salen)] complex, with the exception of a low-intensity absorption band B_1 (an additional vacant π* molecular orbital), which is observed in the N 1*s* spectrum of the complex 1.5 eV above the main absorption resonance *B* (lowest unoccupied π* molecular orbital) (Figure 16a). A detailed comparison of the C 1*s* NEXAFS spectra of H_2(Salen) and [Ni(Salen)] made it possible to identify the absorption bands caused by the C 1*s* electron transitions for the ethylenediamine fragment (the ethylene molecule C_2H_4 and the imine functional group –N=C–) designated in Figure 16b by capital dashed letters as well as those for the phenolic C_6H_5OH fragment designated in Figure 16b by capital letters with asterisks. In addition, from a combined analysis of the N 1*s* and C 1*s* spectra, it follows that the ethylenediamine bridge does not change upon passing from free salen to the [Ni(Salen)] complex. However, the O 1*s* NEXAFS spectrum (Figure 16c), in contrast to the N 1*s* and C 1*s* spectra, has undergone significant changes in [Ni(Salen)] compared to H_2(Salen). Narrow low-energy absorption resonances in the [Ni(Salen)] spectrum are associated with transitions of O 1*s* electrons to two vacant antibonding π*-MOs, reflecting the presence of a π-bond with the Ni atom (π-back-donation) and π-conjugation between oxygen atoms and phenolic rings, respectively.

Thus, the NEXAFS and EXAFS spectroscopies are highly informative experimental techniques that provide valuable knowledge about the electronic structure of molecular complexes [M(Salen)] and their polymers, as well as about the structure of the local environment of the atoms under study in these systems. However, from the works cited above, it follows that NEXAFS and EXAFS data are available only for a small number of monomers, ([Co(Salen)], [Cu(Salen)], [Ni(3-CH_3saltMe)], and [Pd(3-CH_3Salen)]), and some polymers, (poly-[Ni(3-CH_3saltMe)] and poly-[Pd(3-CH_3Salen)]). Moreover, NEXAFS data for the ligand atoms (nitrogen, oxygen, and carbon) are known only for the H_2(Salen) molecule and the monomer [Ni(Salen)] complex.

3.3. Atomic and Electronic Structure of Composites Based on [M(Salen)] and Carbon Nanomaterials

A detailed examination of the relevant literature [3,8–10,37,42,100–112,114,134–139] showed that TEM, XRD, EDS, Raman, and IR spectroscopy, alongside thermogravimetric analysis and electrochemical methods, are the most commonly used techniques to characterize the structure of composites based on [M(Salen)] and poly-[M(Salen)] with various carbon materials, such as carbon nanotubes, single-walled carbon nanohorns (SWNHs), graphene, graphene oxide (GO), reduced GO (rGO), nitrogen-doped graphene, few-layer graphene (FLG), etc. At the same time, XPS is not widely used for the above-mentioned composites despite the fact that it is the most powerful method for identifying the chemical state of functional atoms in nanostructured composite materials. The currently available XPS data for [M(Salen)]/CNT, [M(Salen)]/GO, poly-[M(Salen)]/CNT, and poly-[M(Salen)]/FLG, etc., are presented in Table 4.

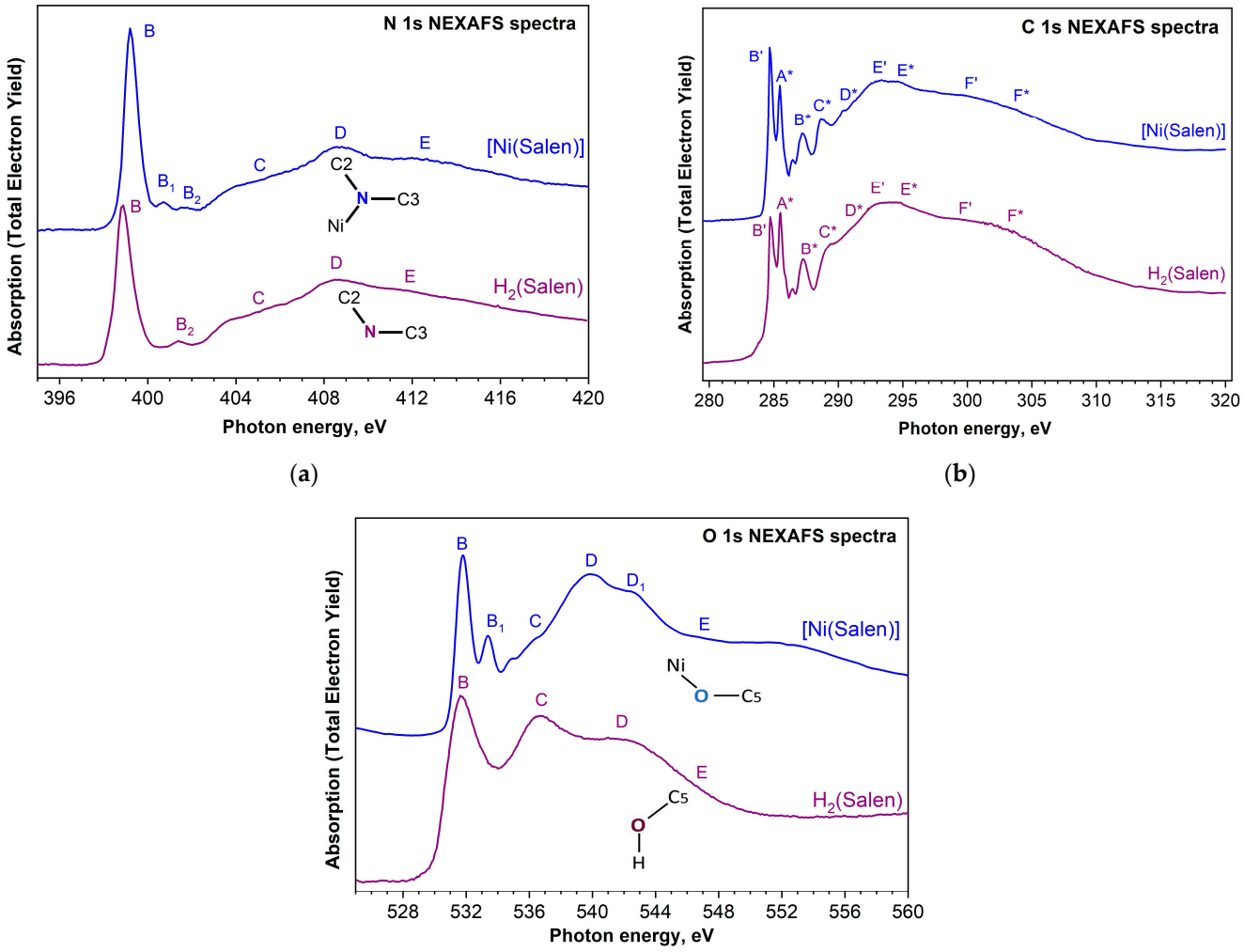

Figure 16. N 1*s* (**a**), C 1*s* (**b**), and O 1*s* (**c**) NEXAFS spectra of the H_2(Salen) ligand (purple line) and the [Ni(Salen)] complex (blue line). In the N 1*s* and O 1*s* spectra, the capital letters denote X-ray absorption bands due to the N 1*s* and O 1s electron transitions to unoccupied electronic states, respectively. In the case of C 1*s* spectra, the capital letters with dashes and asterisks denote X-ray absorption bands due to the transitions of C 1*s* electrons of ethylenediamine and phenolic groups to unoccupied electronic states, respectively [46].

In works [103,104,134,135,137,138], XPS data were published on monomeric complexes [M($(OH)_2$-salen)] and [M(Salen)] with various complexing metals, Mn, Co, Cu, and Ni, as well as with vanadium oxide (VO), which were deposited on the surface of MWCNTs functionalized by chlorination [103,134,135,137,138] or by adding NH_2 amino groups [104]. In other studies, the XPS measurements on composites based on poly-[Co-Tos-(Salen)] (Tos–p-toluenesulfonic anion, $CH_3C_6H_3SO_2$) [105] and [Ni(salphen)] polymers deposited on a CNT surface [8] as well as poly-[Ni(3-CH_3-salen)] electrochemically deposited on N-doped FLG (N-FLG) [37] are presented. XPS studies of GO-based composites with deposited [M(Salen)] complexes with the metals Co, Cu, Fe, and Ni and also with a VO are described by Z. Li et al. [108,110], W.-C. Wei et al. [109], and Q. Zhao et al. [111]. The composites investigated in these works were synthesized using preliminary functionalization of GO surface with amino NH_2 (NH_2-GO) [108–110] and with 3-(Aminopropyl) trimethoxysilane (APTMS) [111]. For clarity and subsequent comparison of changes, all XPS data measured in [8,37,101,103–105,108–111,134,135,137,138] are summarized in Table 5.

Table 4. XPS data overview of composites based on [M(Salen)] complex with different carbon nanostructures.

Sample	Measured Photoelectron Region	Photon Source, Spectrometer	Spectra Calibration	Functionalization Method of Carbon Surface	Ref.
[Mn($(OH)_2$-salen)]/MWCNTs [Co($(OH)_2$-salen)]/MWCNTs [Ni($(OH)_2$-salen)]/MWCNTs [Cu($(OH)_2$-salen)]/MWCNTs [VO($(OH)_2$-salen)]/MWCNTs	Survey, O 1*s*, Mn 2*p* Survey, O 1s, Co 2*p* Survey, O 1s, Ni 2*p* Survey, O 1*s*, Cu 2*p* Survey, O 1*s*, V 2*p*	Mg Kα PHI-5702	not specified	chlorination	[134] [135] [103] [137] [138]
[Co(Salen)]/MWCNTs [Cu(Salen)]/MWCNTs	Survey, N 1*s*, Co 2*p* Survey, Cu 2*p*	Al Kα ESCALAB 250Xi	C 1s-284.6	functionalization with amino (NH_2-CNT))	[104]
poly-[Ni(salphen)]/MWCNTs	Survey, Ni 2*p*	not specified	not specified	homogeneous suspension of MWCNTs and N-methyl-2-pyrrolidone	[8]
poly-[Co-Tos-(Salen)]/CNTs	Survey, Co 2*p*	not specified	not specified	ethylene diamine treatment	[105]
[Co(Salen)]/SWNHs	Survey, N 1*s*, Co 2*p*	Al Kα ESCALAB MKII	not specified	sonicating and stirring a toluene solution of Co-Salen and SWNHs	[101]
[Co(Salen)]/GO [Cu(Salen)]/GO [VO(Salen)]/GO [Fe(Salen)]/GO [Ni(Salen)]/GO	Survey Survey C 1*s*, V 2*p* C 1*s*, Fe 2*p* C 1*s*, N 1*s*	Al Kα ESCALAB 250 Al Kα Kratos AXIS Ultra HSA	not specified	functionalization with amino NH_2 (NH_2–GO)	[110] [108] [109]
[Cu(Salen)]/GO	Survey, N 1*s*, Cu 2*p*	not specified		functionalization with 3-(Aminopropyl) trimethoxysilane (APTMS)	[111]
poly-[Ni(3-CH_3-Salen)]/N-FLG	C 1*s*, O 1s, N 1*s*, Ni 2*p*, Cl 2*p*	Al Kα CEMUP	not specified	nitrogen doping using CVD method with additional ammonia precursor	[37]

Table 5. Energy position E_{bin} of peaks in C 1*s*, N 1*s*, O 1*s*, and M $2p_{3/2}$ (Mn, Co, Ni, Cu, V, and Fe) PE spectra of composites.

Sample	Peaks Position, eV									Ref.
	C 1*s*		N 1*s*		O 1*s*			M 2*p*		
	H^1 Peak	L^2 Peak	H^1 Peak	L^2 Peak	–CO–	–C–O–C– or –C–O–N–	–C–O–M–	$2p_{3/2}$	dE^3	
[Mn($(OH)_2$-salen)]/MWCNTs	–	–	–	–	532.7	531.2	529.9	640.0	11.4	[134]
[Co($(OH)_2$-salen)]/MWCNTs	–	–	–	–	532.3	531.2	529.7	780.4	14.7	[135]
[Ni($(OH)_2$-salen)]/MWCNTs	–	–	–	–	532.8	531.4	529.9	854.1	21.2	[103]
[Cu($(OH)_2$-salen)]/MWCNTs	–	–	–	–	532.5	531.4	529.9	934.2	20	[137]
[VO($(OH)_2$-salen)]/MWCNTs	–	–	–	–	532.6	531.5	530.0	515	–	[138]
[Co(Salen)]/MWCNTs	–	–	402	399.5	–	–	–	~781.5	14.7	[104]
[Cu(Salen)]/MWCNTs	–	–	–	–	–	–	–	~934.4	19.9	[104]
Poly-[Ni(salphen)]/MWCNTs	–	–	–	–	–	–	–	~855	~18	[8]
Poly-[Co-Tos-(Salen)]/CNTs,	–	–	–	–	–	–	–	~780.7	~15.2	[105]
[Co(Salen)]/SWNHs	–	–	~400	–	–	–	–	~780.9	~15	[101]
[VO(Salen)]/GO [Fe(Salen)]/GO	284.7 284.8	286.7 286.6	– –	– –	– –	– –	– –	517.1 711.8	~7 13.5	[108]
[Ni(Salen)]/GO	284.6	286.6	401.8	399.5	–	–	–	–	–	[109]
[Ni(Salen)]/rGO	284.6	286.5	401.8	399.5	–	–	–	–	–	[109]
[Cu(Salen)]/GO	–	–	~401	~399.2	–	–	–	~954	~19.9	[111]
Poly-[Ni(3-CH3-Salen)]/N-FLG	284.6	285.9 286.9	401.3 400.4	399.4	533.1	531.5		872.5	17.2	[37]

H^1—higher-intensity peak. L^2—lower-intensity peak. dE^3 = E2$p_{1/2}$ − E2$p_{3/2}$—energy distance between $2p_{1/2}$ and $2p_{3/2}$ photoemission lines.

In the above-mentioned works, the authors used different approximating functions and approaches to fit the C 1*s* and N 1*s* PE spectra, which resulted in a different number

of components and a spread in the value of their energy positions as well as FWHM (full width at half maximum). However, in almost all C 1*s* and N 1*s* spectra, regardless of the fitting method, two main peaks can be identified. The first peak (H) has a higher intensity, while the second one (L) has a lower intensity or in some cases appears as a shoulder on the high binding energy side. In the C 1*s* spectra, an intense peak is associated with the C atoms of the benzene ring of salen and carbon material, and the subsequent higher energy (less intense peak) is attributed to carbon atoms in the –C–O–H and –C–N–H bonds of the phenolic and ethylenediamine moieties as well as surface C–O or C–N groups of carbon material, respectively (Figure 17a). In addition, additional low-intensity peaks in the region of high binding energies are possible, associated with C=O groups on the surface of the carbon nanomaterial.

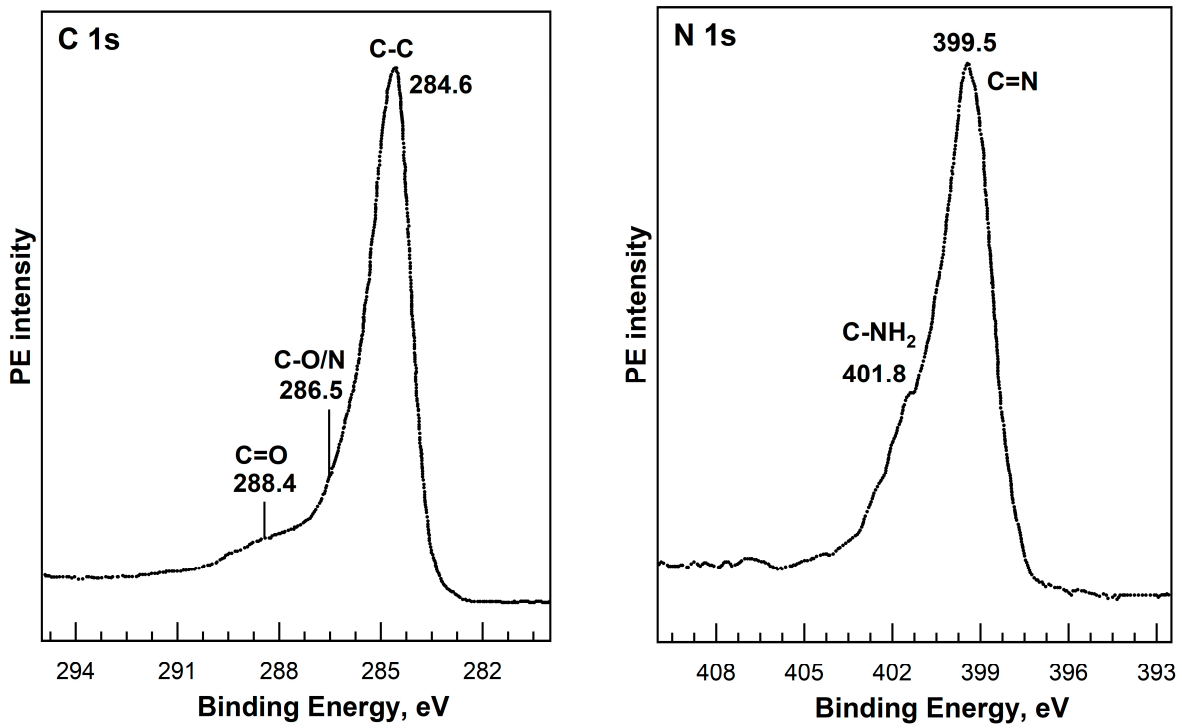

(**a**) (**b**)

Figure 17. C 1*s* (**a**) and N 1*s* (**b**) PE spectra of [Ni(Salen)]/rGO. Adapted from Ref. [109] with permission.

As for the N 1*s* spectra, the first peak of high intensity is attributed to atoms in the metal–salen complexes, and the second peak of low intensity is associated with the contribution from the N dopant or amino NH_2 groups fixed on the surface of the carbon nanomaterial after its functionalization (Figure 17b). Comparing the data in Table 5, we can conclude that differences in the energy positions of the main peaks in the C 1*s* and N 1*s* PE spectra may be a consequence of various factors, including energy calibration of the binding energy scale, redistribution of electron density between metal (V, Fe, or Ni) and salen ligand atoms, and the influence of added N-containing groups when treating the surface of nanocarbon. In turn, O 1*s* PE spectra are usually fitted with two [37] or three [103,134,135,137,138] components of comparable intensities and associated with O 1s binding energies in oxygen-containing groups –CO– (532.0–532.7 eV), –C–O–C– (531.2–531.5 eV), and –C–O–M– (529.7–530.0 eV).

Let us now move on to consider the most frequently encountered M 2*p* PE spectra of composites with [M(Salen)] complexes in the literature. Unfortunately, the method of energy calibration of M 2*p* PE spectra in the studies presented in Table 5 is often not specified. Therefore, it is not possible to carry out a comparative analysis of the energy position of the

most intense $2p_{3/2}$ PE line to estimate the degree of oxidation of the complexing metal in various [M(Salen)] complexes. At the same time, it is known that a change in the energy distance between the $2p_{3/2}$ and $2p_{1/2}$ lines (dE) in the M $2p$ PE spectra allows one to estimate the degree of oxidation of metals [139]. In view of the above, in order to carry out a more accurate spectral analysis, we assessed not only the energy position of the $2p_{3/2}$ line but also the dE values, which are given in Table 5. So, for [M(Salen)] with Co, Cu, and Ni complexing metals, the value of the dE parameter is in the ranges of 14.7–15.2, 19.9–20, and 17.2–21.2 eV, respectively. It is important to note that the change in dE for the same complexing metal in composites ([M(Salen)]/MWCNTs) can be explained by a change in the oxidation state of the metal due to the additional addition of functional groups to the salen ligand (Salfen, $(OH)_2$-salen, Toc-(Salen), (3-CH_3-Salen)). It is noteworthy that composites with [Cu(Salen)] supported on carbon materials showed the same value of dE = 19.9 eV for different carbon substrates (MWCNTs and GO), indicating that the carbon substrate has little effect on the charge state of the complexing metal in [Cu(Salen)].

It should be noted that XPS studies of [M(Salen)]/(carbon nanomaterials) composites are not systematic, which leads to an incomplete understanding of changes in the chemical (charge) state of the metal atom and the salen ligand atoms in [M(Salen)] monomers and poly-[M(Salen)] during their deposition on the surface of carbon materials. In addition, the lack of a comprehensive approach, including the study of XPS spectra of all elements in the composite, does not allow us to assess the features of the interaction of nanostructured carbon materials with [M(Salen)] complexes and their derivatives. It is important to note that studies of unoccupied electron states using X-ray absorption spectroscopy, as well as those of the occupied valence electron states using valence photoemission, are still missing for these composites. As a consequence, the lack of these data significantly complicates the development of new highly efficient nanocomposites for various purposes based on monomeric salen complexes or their polymer derivatives and carbon nanostructures.

4. Conclusions

This review summarizes information on the study of [M(Salen)] complexes as well as electrically conductive redox polymers and composites based on them with carbon nanostructures using highly informative X-ray spectroscopy methods, such as XPS, VB PES, NEXAFS, and EXAFS. It is shown that research in recent years is characterized by individual attempts to use these methods to obtain information about the chemical state of functional atoms in [M(Salen)] monomers and their polymers, as well as about the atomic structure of these polyatomic systems. However, the largest number of results were obtained using the XPS method, while VB PES, NEXAFS, and EXAFS were rarely used. At the same time, existing studies using the above techniques demonstrate the possibility of obtaining information about the local atomic and electronic structure of complexes and polymers, which is necessary for a deep understanding and detailed description of the properties of these polyatomic systems.

In the case of composites based on [M(Salen)] complexes and their polymers with carbon nanostructures (carbon nanotubes and graphene), only a limited amount of XPS data are available for some functional atoms. It is significant that these data are usually obtained with low energy resolution and insufficient statistics, and they are not systematic. In addition, there are also problems with relating the positions of photoelectron lines in the XPS spectra to the binding energy scale caused by different methods of energy calibration of the same spectra in different experiments. It is important to note that VB PES, NEXAFS, and EXAFS studies of these systems are currently completely missing. To summarize, it is important to say that the lack of comprehensive XPS, VB PES, NEXAFS, and EXAFS studies limits the understanding of the details of the polymerization processes of monomer molecules [M(Salen)] as well as the mechanisms of interaction of monomers and their polymers with carbon nanomaterials when developing new nanocomposites for various purposes.

Author Contributions: Conceptualization, P.M.K. and A.S.V.; research supervision, A.S.V.; visualization, P.M.K. and O.V.P.; writing—original draft, P.M.K., O.V.P. and A.S.V.; writing—review and editing P.M.K. All authors have read and agreed to the published version of the manuscript.

Funding: This work was funded by the Russian Science Foundation, grant number 21-72-10029. https://www.rscf.ru/en/project/21-72-10029/ (accessed on 25 January 2024).

Data Availability Statement: Not applicable.

Acknowledgments: The authors express their gratitude to Ksenia Bakina and Vyacheslav Gaas for technical assistance in preparing the manuscript. This article is dedicated to the 300th anniversary of the founding of St. Petersburg University.

Conflicts of Interest: The authors declare no conflicts of interest.

References

1. Soos, Z.; Mukhopadhyay, D.; Painelli, A.; Girlando, A. *Handbook of Conducting Polymers*, 2nd ed.; Revised and Expanded; CRC Press: Boca Raton, FL, USA, 1998; pp. 165–208. ISBN 0824700503.
2. Leung, A.C.W.; MacLachlan, M.J. Schiff Base Complexes in Macromolecules. *J. Inorg. Organomet. Polym. Mater.* **2007**, *17*, 57–89. [CrossRef]
3. Li, X.; Li, J.; Deng, F.; Kang, F. Enhanced Electrochemical Performance of Nitrogen-Doped Graphene and Poly[Ni(Salen)] Composite Electrodes for Supercapacitors. *Ionics* **2018**, *24*, 3143–3153. [CrossRef]
4. Zhang, Y.; Li, J.; Gao, F.; Kang, F.; Wang, X.; Ye, F.; Yang, J. Electropolymerization and Electrochemical Performance of Salen-Type Redox Polymer on Different Carbon Supports for Supercapacitors. *Electrochim. Acta* **2012**, *76*, 1–7. [CrossRef]
5. Zhu, Z.; Lu, J.; Li, X.; Xu, G.; Chen, C.; Li, J. Effects of Potential Modes on Performances of Electrodeposited Poly[Ni(Salen)]/MWCNTs Composite as Supercapacitor Electrode Material. *Electrochemistry* **2016**, *84*, 427–431. [CrossRef]
6. Alekseeva, E.; Stelmashuk, T.; Ershov, V.; Levin, O. Low-Temperature Energy Storage Performance of NiSalen Type Polymer and It's Composite with SWCNT. *Electrochim. Acta* **2021**, *383*, 138309:1–138309:10. [CrossRef]
7. Li, J.L.; Gao, F.; Zhang, Y.K.; Kang, F.Y.; Wang, X.D.; Ye, F.; Yang, J. Electropolymerization of Ni(Salen) on Carbon Nanotube Carrier as a Capacitive Material by Pulse Potentiostatic Method. *Sci. China Chem.* **2012**, *55*, 1338–1344. [CrossRef]
8. Chen, C.; Zhu, Z.; Li, X.; Li, J. Electropolymerization and Energy Storage of Poly[Ni(Salphen)]/MWCNT Composite Materials for Supercapacitors. *J. Appl. Polym. Sci.* **2017**, *134*, 44464:1–44464:8. [CrossRef]
9. Tedim, J.; Gonçalves, F.; Pereira, M.F.R.; Figueiredo, J.L.; Moura, C.; Freire, C.; Hillman, A.R. Preparation and Characterization of Poly[Ni(Salen)(Crown Receptor)]/Multi-Walled Carbon Nanotube Composite Films. *Electrochim. Acta* **2008**, *53*, 6722–6731. [CrossRef]
10. Moradi, L.; Rezaeei Bina, M.; Partovi, T. New Strategy for Chemically Attachment of Schiff Base Complexes on Multiwalled Carbon Nanotubes Surfaces. *Curr. Chem. Lett.* **2014**, *3*, 147–156. [CrossRef]
11. Vasil'eva, S.V.; Balashev, K.P.; Timonov, A.M. Effects of the Nature of the Ligand and Solvent on the Electrooxidation of Complexes Formed by Nickel and Schiff's Bases. *Russ. J. Electrochem.* **1998**, *34*, 978–983.
12. Vilas-Boas, M.; Santos, I.C.; Henderson, M.J.; Freire, C.; Hillman, A.R.; Vieil, E. Electrochemical Behavior of a New Precursor for the Design of Poly[Ni(Salen)]-Based Modified Electrodes. *Langmuir* **2003**, *19*, 7460–7468. [CrossRef]
13. Hamnett, A.; Abel, J.; Eameaim, J.; Christensen, P.; Timonov, A.; Vasilyeva, S. A Study of the Polymerisation and Electrochemical Cycling of Pd Methoxy- Salen Derivatives Using Fast Ellipsometry and FT-Infrared Spectroscopy. *Phys. Chem. Chem. Phys.* **1999**, *1*, 5147–5156. [CrossRef]
14. Vilas-Boas, M.; Henderson, M.J.; Freire, C.; Hillman, A.R.; Vieil, E. A Combined Electrochemical Quartz-Crystal Microbalance Probe Beam Deflection (EQCM-PBD) Study of Solvent and Ion Transfers at a Poly[Ni(SaltMe)]-Modified Electrode during Redox Switching. *Chem.-Eur. J.* **2000**, *6*, 1160–1167. [CrossRef]
15. Krasikova, S.A.; Besedina, M.A.; Karushev, M.P.; Dmitrieva, E.A.; Timonov, A.M. In Situ Electrochemical Microbalance Studies of Polymerization and Redox Processes in Polymeric Complexes of Transition Metals with Schiff Bases. *Russ. J. Electrochem.* **2010**, *46*, 218–226. [CrossRef]
16. Dmitrieva, E.A.; Logvinov, S.A.; Kurdakova, V.V.; Kondrat'ev, V.V.; Malev, V.V.; Timonov, A.M. Redox Polymer Poly-N,N′-2,3-Dimethylbutane-2,3-Diyl-Bis(Salicylideniminato)Nickel: An Impedance Spectroscopy Study. *Russ. J. Electrochem.* **2005**, *41*, 381–387. [CrossRef]
17. Yan, G.; Li, J.; Zhang, Y.; Gao, F.; Kang, F. Electrochemical Polymerization and Energy Storage for Poly[Ni(Salen)] as Supercapacitor Electrode Material. *J. Phys. Chem. C* **2014**, *118*, 9911–9917. [CrossRef]
18. Girichev, G.V.; Giricheva, N.I.; Kuzmina, N.P.; Levina, Y.S.; Rogachev, A.Y. Molecular Structure of $NiO_2N_2C_{16}H_{14}$ from Gas-Phase Electron Diffraction and Quantum Chemical Data. *J. Struct. Chem.* **2005**, *46*, 813–823. [CrossRef]
19. Goldsby, K.A.; Blaho, J.K.; Hoferkamp, L.A. Oxidation of Nickel(II) Bis(Salicylaldimine) Complexes: Solvent Control of the Ultimate Redox Site. *Polyhedron* **1989**, *8*, 113–115. [CrossRef]
20. Hoferkamp, L.A.; Goldsby, K.A. Surface-Modified Electrodes Based on Nickel(II) and Copper(II) Bis(Salicylaldimine) Complexes. *Chem. Mater.* **1989**, *1*, 348–352. [CrossRef]

21. Vasil'ev, V.; Popeko, I.E.; Timonov, A.; Shagisultanova, G.A. The Electrochemical Behavior of Palladium(II) Complexes with Schift Bases and the Synthesis of a Mixed-Valence Pd(II)-Pd(IV) Complex. *Russ. J. Inorg. Chem.* **1990**, *35*, 523–525.
22. Dahm, C.E.; Peters, D.G.; Simonet, J. Electrochemical and Spectroscopic Characterization of Anodically Formed Nickel Salen Polymer Films on Glassy Carbon, Platinum, and Optically Transparent Tin Oxide Electrodes in Acetonitrile Containing Tetramethylammonium Tetrafluoroborate. *J. Electroanal. Chem.* **1996**, *410*, 163–171. [CrossRef]
23. Audebert, P.; Capdevielle, P.; Maumy, M. Redox and Conducting Polymers Based on Salen-Type Metal Units; Electrochemical Study and Some Characteristics. *New J. Chem.* **1992**, *16*, 697–703.
24. Vilas-Boas, M.; Freire, C.; De Castro, B.; Christensen, P.A.; Hillman, A.R. New Insights into the Structure and Properties of Electroactive Polymer Films Derived from [Ni(Salen)]. *Inorg. Chem.* **1997**, *36*, 4919–4929. [CrossRef]
25. Vilas-Boas, M.; Freire, C.; de Castro, B.; Christensen, P.A.; Hillman, A.R. Spectroelectrochemical Characterisation of Poly[Ni(SaltMe)]-Modified Electrodes. *Chemistry* **2001**, *7*, 139–150. [CrossRef]
26. Semenistaya, T.V.; Shagisultanova, G.A. Synthesis of New Cu(II), Ni(II), Pd(II), and Pt(II) Complexes and Conducting Photosensitive Polymers Based on Them. *Russ. J. Inorg. Chem.* **2003**, *48*, 520–527.
27. Tedim, J.; Carneiro, A.; Bessada, R.; Patrício, S.; Magalhães, A.L.; Freire, C.; Gurman, S.J.; Hillman, A.R. Correlating Structure and Ion Recognition Properties of [Ni(Salen)]-Based Polymer Films. *J. Electroanal. Chem.* **2007**, *610*, 46–56. [CrossRef]
28. Mukherjee, P.; Biswas, C.; Drew, M.G.B.; Ghosh, A. Structural Variations in Ni(II) Complexes of Salen Type Di-Schiff Base Ligands. *Polyhedron* **2007**, *26*, 3121–3128. [CrossRef]
29. Storr, T.; Wasinger, E.C.; Pratt, R.C.; Stack, T.D.P. The Geometric and Electronic Structure of a One-Electron-Oxidized Nickel(II) Bis(Salicylidene)Diamine Complex. *Angew. Chem.-Int. Ed.* **2007**, *46*, 5198–5201. [CrossRef]
30. Tedim, J.; Bessada, R.; Patrício, S.; Magalhães, A.L.; Freire, C.; Gorman, S.J.; Hillman, A.R. Unusual Coordination Environment for Barium Cations in Ion Recognition Conducting Poly[Ni(Salen)(Receptor)] Films. *Langmuir* **2008**, *24*, 8998–9005. [CrossRef]
31. Shimazaki, Y.; Arai, N.; Dunn, T.J.; Yajima, T.; Tani, F.; Ramogida, C.F.; Storr, T. Influence of the Chelate Effect on the Electronic Structure of One-Electron Oxidized Group 10 Metal(Ii)-(Disalicylidene)Diamine Complexes. *Dalton Trans.* **2011**, *40*, 2469–2479. [CrossRef]
32. Tedim, J.; Patrício, S.; Fonseca, J.; Magalhães, A.L.; Moura, C.; Hillman, A.R.; Freire, C. Modulating Spectroelectrochemical Properties of [Ni(Salen)] Polymeric Films at Molecular Level. *Synth. Met.* **2011**, *161*, 680–691. [CrossRef]
33. Levin, O.V.; Karushev, M.P.; Timonov, A.M.; Alekseeva, E.V.; Zhang, S.; Malev, V.V. Charge Transfer Processes on Electrodes Modified by Polymer Films of Metal Complexes with Schiff Bases. *Electrochim. Acta* **2013**, *109*, 153–161. [CrossRef]
34. Sizov, V.V.; Novozhilova, M.V.; Alekseeva, E.V.; Karushev, M.P.; Timonov, A.M.; Eliseeva, S.N.; Vanin, A.A.; Malev, V.V.; Levin, O.V. Redox Transformations in Electroactive Polymer Films Derived from Complexes of Nickel with SalEn-Type Ligands: Computational, EQCM, and Spectroelectrochemical Study. *J. Solid State Electrochem.* **2015**, *19*, 453–468. [CrossRef]
35. Nunes, M.; Araújo, M.; Fonseca, J.; Moura, C.; Hillman, R.; Freire, C. High-Performance Electrochromic Devices Based on Poly[Ni(Salen)]-Type Polymer Films. *ACS Appl. Mater. Interfaces* **2016**, *8*, 14231–14243. [CrossRef]
36. Vereshchagin, A.A.; Sizov, V.V.; Verjuzhskij, M.S.; Hrom, S.I.; Volkov, A.I.; Danilova, J.S.; Novozhilova, M.V.; Laaksonen, A.; Levin, O.V. Interaction of Amines with Electrodes Modified by Polymeric Complexes of Ni with Salen-Type Ligands. *Electrochim. Acta* **2016**, *211*, 726–734. [CrossRef]
37. Nunes, M.; Araújo, M.; Bacsa, R.; Ferreira, R.V.; Castillejos, E.; Serp, P.; Hillman, A.R.; Freire, C. N-Doped Few-Layered Graphene-PolyNi Complex Nanocomposite with Excellent Electrochromic Properties. *Carbon* **2017**, *120*, 32–43. [CrossRef]
38. Alekseeva, E.V.; Chepurnaya, I.A.; Malev, V.V.; Timonov, A.M.; Levin, O.V. Polymeric Nickel Complexes with Salen-Type Ligands for Modification of Supercapacitor Electrodes: Impedance Studies of Charge Transfer and Storage Properties. *Electrochim. Acta* **2017**, *225*, 378–391. [CrossRef]
39. Shagisultanova, G.A.; Shchukarev, A.V.; Semenistaya, T.V. Possibilities of X-ray Photoelectron Spectroscopy in Studying the Structure and Properties of Polymers Based on Transition Metal Complexes with Schiff Bases. *Russ. J. Inorg. Chem.* **2005**, *50*, 912–924.
40. Fonseca, J.; Tedim, J.; Biernacki, K.; Magalhães, A.L.; Gurman, S.J.; Freire, C.; Hillman, A.R. Structural and Electrochemical Characterisation of [Pd(Salen)]-Type Conducting Polymer Films. *Electrochim. Acta* **2010**, *55*, 7726–7736. [CrossRef]
41. Dmitrieva, E.; Rosenkranz, M.; Danilova, J.S.; Smirnova, E.A.; Karushev, M.P.; Chepurnaya, I.A.; Timonov, A.M. Radical Formation in Polymeric Nickel Complexes with N_2O_2 Schiff Base Ligands: An in Situ ESR and UV–Vis–NIR Spectroelectrochemical Study. *Electrochim. Acta* **2018**, *283*, 1742–1752. [CrossRef]
42. Chen, C.; Li, X.; Deng, F.; Li, J. Electropolymerization and Electrochemical Behavior of Nickel Schiff Base Complexes with Different Groups between Imine Linkages. *RSC Adv.* **2016**, *6*, 79894–79899. [CrossRef]
43. Alekseeva, E.V.; Vereshchagin, A.A.; Novozhilova, M.V.; Panjwani, N.A.; Novoselova, J.V.; Lukyanov, D.A.; Beletskii, E.V.; Behrends, J.; Sizov, V.V.; Levin, O.V. Uncovering the Mechanism of Water-Promoted Electrochemical Degradation of NiSalen Polymers. *J. Electroanal. Chem.* **2023**, *935*, 117310:1–117310:16. [CrossRef]
44. Vereschagin, A.A.; Sizov, V.V.; Vlasov, P.S.; Alekseeva, E.V.; Konev, A.S.; Levin, O.V. Water-Stable [Ni(Salen)]-Type Electrode Material Based on Phenylazosubstituted Salicylic Aldehyde Imine Ligand. *New J. Chem.* **2017**, *41*, 13918–13928. [CrossRef]
45. Svirskiy, G.I.; Generalov, A.V.; Vinogradov, N.A.; Brykalova, X.O.; Vereshchagin, A.V.; Levin, O.V.; Lyalin, A.G.; Preobrajenski, A.B.; Vinogradov, A.S. Electronic Structure of the [Ni(Salen)] Complex Studied by Core-Level Spectroscopies. *Phys. Chem. Chem. Phys.* **2021**, *23*, 11015–11027. [CrossRef] [PubMed]

46. Korusenko, P.M.; Petrova, O.V.; Vereshchagin, A.A.; Katin, K.P.; Levin, O.V.; Nekipelov, S.V.; Sivkov, D.V.; Sivkov, V.N.; Vinogradov, A.S. A Comparative XPS, UV PES, NEXAFS, and DFT Study of the Electronic Structure of the Salen Ligand in the H2(Salen) Molecule and the [Ni(Salen)] Complex. *Int. J. Mol. Sci.* **2023**, *24*, 9868. [CrossRef]
47. Chepurnaya, I.A.; Logvinov, S.A.; Karushev, M.P.; Timonov, A.M.; Malev, V.V. Modification of Supercapacitor Electrodes with Polymer Metallocomplexes: Methods and Results. *Russ. J. Electrochem.* **2012**, *48*, 538–544. [CrossRef]
48. Li, X.; Li, J.; Kang, F. Enhanced Electrochemical Performance of Salen-Type Transition Metal Polymer with Electron-Donating Substituents. *Ionics* **2019**, *25*, 1045–1055. [CrossRef]
49. Deng, F.; Li, X.; Ding, F.; Niu, B.; Li, J. Pseudocapacitive Energy Storage in Schiff Base Polymer with Salphen-Type Ligands. *J. Phys. Chem. C* **2018**, *122*, 5325–5333. [CrossRef]
50. Burness, J.H.; Dillard, J.G.; Taylor, L.T. An X-ray Photoelectron Spectroscopic Study of Cobalt(II) Schiff Base Complexes and Their Oxygenation Products. *J. Am. Chem. Soc.* **1975**, *97*, 6080–6088. [CrossRef]
51. Dillard, J.G.; Taylor, L.T. X-ray Photoelectron Spectroscopic Study of Schiff Base Metal Complexes. *J. Electron. Spectros Relat. Phenom.* **1974**, *3*, 455–460. [CrossRef]
52. Kshirsagar, V.S.; Garade, A.C.; Mane, R.B.; Patil, K.R.; Yamaguchi, A.; Shirai, M.; Rode, C.V. Characterization of Clay Intercalated Cobalt-Salen Catalysts for the Oxidation of p-Cresol. *Appl. Catal. A Gen.* **2009**, *370*, 16–23. [CrossRef]
53. Korusenko, P.M.; Koroleva, A.V.; Vereshchagin, A.A.; Sivkov, D.V.; Petrova, O.V.; Levin, O.V.; Vinogradov, A.S. The Valence Band Structure of the [Ni(Salen)] Complex: An Ultraviolet, Soft X-ray and Resonant Photoemission Spectroscopy Study. *Int. J. Mol. Sci.* **2022**, *23*, 6207. [CrossRef]
54. Gaur, A.; Shrivastava, B.D.; Srivastava, K.; Prasad, J.; Singh, S.K. XAFS Investigations of Copper(II) Complexes with Tetradentate Schiff Base Ligands. *X-ray Spectrom.* **2012**, *41*, 384–392. [CrossRef]
55. Johnson, C.; Long, B.; Nguyen, J.G.; Day, V.W.; Borovik, A.S.; Subramaniam, B.; Guzman, J. Correlation between Active Center Structure and Enhanced Dioxygen Binding in Co(Salen) Nanoparticles: Characterization by in Situ Infrared, Raman, and X-ray Absorption Spectroscopies. *J. Phys. Chem. C* **2008**, *112*, 12272–12281. [CrossRef]
56. Storr, T.; Verma, P.; Pratt, R.C.; Wasinger, E.C.; Shimazaki, Y.; Stack, T.D.P. Defining the Electronic and Geometric Structure of One-Electron Oxidized Copper-Bis-Phenoxide Complexes. *J. Am. Chem. Soc.* **2008**, *130*, 15448–15459. [CrossRef] [PubMed]
57. Sliznev, V.V.; Girichev, G.V. A Theoretical Study of Keto-Enol Isomerism and Internal Rotation in the H2Salen Molecule, N,N′-Ethylene-Bis(Salicylidenimine)—Schiff Base. *J. Struct. Chem.* **2011**, *52*, 16–26. [CrossRef]
58. Freire, C.; Nunes, M.; Pereira, C.; Fernandes, D.M.; Peixoto, A.F.; Rocha, M. Metallo(Salen) Complexes as Versatile Building Blocks for the Fabrication of Molecular Materials and Devices with Tuned Properties. *Coord. Chem. Rev.* **2019**, *394*, 104–134. [CrossRef]
59. Clarke, R.M.; Herasymchuk, K.; Storr, T. Electronic Structure Elucidation in Oxidized Metal–Salen Complexes. *Coord. Chem. Rev.* **2017**, *352*, 67–82. [CrossRef]
60. Sunday Nworie, F. Bis(Salicylidene)Ethylenediamine(Salen) and Bis(Salicylidene)Ethylenediamine-Metal Complexes: From Structure to Biological Activity. *J. Anal. Pharm. Res.* **2016**, *3*, 00076. [CrossRef]
61. Chepurnaya, I.A.; Karushev, M.P.; Alekseeva, E.V.; Lukyanov, D.A.; Levin, O.V. Redox-Conducting Polymers Based on Metal-*Salen* Complexes for Energy Storage Applications. *Pure Appl. Chem.* **2020**, *92*, 1239–1258. [CrossRef]
62. Shagisultanova, G.A.; Ardasheva, L.P. Electrochemical Synthesis of Thin Films of Polymers Derived from [NiSalen] and [NiSalphen]. *Russ. J. Appl. Chem.* **2003**, *76*, 1626–1630. [CrossRef]
63. Egbedina, A.O.; Bolade, O.P.; Ewuzie, U.; Lima, E.C. Emerging Trends in the Application of Carbon-Based Materials: A Review. *J. Environ. Chem. Eng.* **2022**, *10*, 107260. [CrossRef]
64. Ouyang, J. Applications of Carbon Nanotubes and Graphene for Third-Generation Solar Cells and Fuel Cells. *Nano Mater. Sci.* **2019**, *1*, 77–90. [CrossRef]
65. Yuan, W.; Zhang, Y.; Cheng, L.; Wu, H.; Zheng, L.; Zhao, D. The Applications of Carbon Nanotubes and Graphene in Advanced Rechargeable Lithium Batteries. *J. Mater. Chem. A Mater.* **2016**, *4*, 8932–8951. [CrossRef]
66. Gopiraman, M.; Soo Kim, I. Carbon Nanocomposites: Preparation and Its Application in Catalytic Organic Transformations. In *Nanocomposites—Recent Evolutions*; IntechOpen: Rijeka, Croatia, 2019; pp. 17–43.
67. Zhu, Z. An Overview of Carbon Nanotubes and Graphene for Biosensing Applications. *Nanomicro Lett.* **2017**, *9*, 25. [CrossRef] [PubMed]
68. Onyancha, R.B.; Aigbe, U.O.; Ukhurebor, K.E.; Muchiri, P.W. Facile Synthesis and Applications of Carbon Nanotubes in Heavy-Metal Remediation and Biomedical Fields: A Comprehensive Review. *J. Mol. Struct.* **2021**, *1238*, 130462. [CrossRef]
69. Albers, P.W.; Leich, V.; Ramirez-Cuesta, A.J.; Cheng, Y.; Hönig, J.; Parker, S.F. The Characterisation of Commercial 2D Carbons: Graphene, Graphene Oxide and Reduced Graphene Oxide. *Mater. Adv.* **2022**, *3*, 2810–2826. [CrossRef]
70. Kumar, A.; Sharma, K.; Dixit, A.R. A Review on the Mechanical Properties of Polymer Composites Reinforced by Carbon Nanotubes and Graphene. *Carbon. Lett.* **2021**, *31*, 149–165. [CrossRef]
71. Onyancha, R.B.; Ukhurebor, K.E.; Aigbe, U.O.; Osibote, O.A.; Kusuma, H.S.; Darmokoesoemo, H. A Methodical Review on Carbon-Based Nanomaterials in Energy-Related Applications. *Adsorpt. Sci. Technol.* **2022**, *2022*, 1–21. [CrossRef]
72. Zeng, Y.; Li, T.; Yao, Y.; Li, T.; Hu, L.; Marconnet, A. Thermally Conductive Reduced Graphene Oxide Thin Films for Extreme Temperature Sensors. *Adv. Funct. Mater.* **2019**, *29*, 1901388. [CrossRef]
73. Chen, J.; Li, L. Thermal Conductivity of Graphene Oxide: A Molecular Dynamics Study. *JETP Lett.* **2020**, *112*, 117–121. [CrossRef]
74. Iijima, S. Helical Microtubules of Graphitic Carbon. *Nature* **1991**, *354*, 56–58. [CrossRef]

75. Rathinavel, S.; Priyadharshini, K.; Panda, D. A Review on Carbon Nanotube: An Overview of Synthesis, Properties, Functionalization, Characterization, and the Application. *Mater. Sci. Eng. B* **2021**, *268*, 115095:1–115095:28. [CrossRef]
76. Salah, L.S.; Ouslimani, N.; Bousba, D.; Huynen, I.; Danlée, Y.; Aksas, H. Carbon Nanotubes (CNTs) from Synthesis to Functionalized (CNTs) Using Conventional and New Chemical Approaches. *J. Nanomater.* **2021**, *2021*, 4972770. [CrossRef]
77. Moradi, O.; Yari, M.; Zare, K.; Mirza, B.; Najafi, F. Carbon Nanotubes: A Review of Chemistry Principles and Reactions. *Fuller. Nanotub. Carbon Nanostructures* **2012**, *20*, 138–151. [CrossRef]
78. Zhang, L.; Zhao, X.S. Carbon-Based Materials as Supercapacitor Electrodes. *Chem. Soc. Rev.* **2009**, *38*, 2520–2531. [CrossRef] [PubMed]
79. Kharissova, O.V.; Kharisov, B.I. Variations of Interlayer Spacing in Carbon Nanotubes. *RSC Adv.* **2014**, *4*, 30807–30815. [CrossRef]
80. Kumar Jagadeesan, A.; Thangavelu, K.; Dhananjeyan, V. Carbon Nanotubes: Synthesis, Properties and Applications. In *21st Century Surface Science—A Handbook*; IntechOpen: Rijeka, Croatia, 2020.
81. Jang, J.W. Direct Curvature Measurement of the Compartments in Bamboo-Shaped Multi-Walled Carbon Nanotubes via Scanning Probe Microscopy. *Sci. Rep.* **2021**, *11*, 701. [CrossRef] [PubMed]
82. Taib, N.-A.; Rahman, M.; Matin, M.; Uddin, J.; Bakri, M.K.; Khan, A. A Review on Carbon Nanotubes (CNT): Structure, Synthesis, Purification and Properties for Modern Day Applications. 2021. [CrossRef]
83. Prasek, J.; Drbohlavova, J.; Chomoucka, J.; Hubalek, J.; Jasek, O.; Adam, V.; Kizek, R. Methods for Carbon Nanotubes Synthesis—Review. *J. Mater. Chem.* **2011**, *21*, 15872–15884. [CrossRef]
84. Novoselov, K.S.; Geim, A.K.; Morozov, S.V.; Jiang, D.; Zhang, Y.; Dubonos, S.V.; Grigorieva, I.V.; Firsov, A.A. Electric Field Effect in Atomically Thin Carbon Films. *Science* **2004**, *306*, 666–669. [CrossRef] [PubMed]
85. Purkait, T.; Singh, G.; Singh, M.; Kumar, D.; Dey, R.S. Large Area Few-Layer Graphene with Scalable Preparation from Waste Biomass for High-Performance Supercapacitor. *Sci. Rep.* **2017**, *7*, 15239:1–15239:14. [CrossRef]
86. Zhang, J.; Liu, X.; Zhang, M.; Zhang, R.; Ta, H.Q.; Sun, J.; Wang, W.; Zhu, W.; Fang, T.; Jia, K.; et al. Fast Synthesis of Large-Area Bilayer Graphene Film on Cu. *Nat. Commun.* **2023**, *14*, 3199:1–3199:9. [CrossRef]
87. Podlivaev, A.I.; Grishakov, K.S.; Katin, K.P.; Maslov, M.M. Stone–Wales Bilayer Graphene: Structure, Stability, and Interlayer Heat Transfer. *JETP Lett.* **2021**, *114*, 143–149. [CrossRef]
88. Acik, M.; Chabal, Y.J. Nature of Graphene Edges: A Review. *Jpn. J. Appl. Phys.* **2011**, *50*, 070101. [CrossRef]
89. Yan, J.A.; Chou, M.Y. Oxidation Functional Groups on Graphene: Structural and Electronic Properties. *Phys. Rev. B Condens. Matter Mater. Phys.* **2010**, *82*, 125403. [CrossRef]
90. Suhaimin, N.S.; Hanifah, M.F.R.; wani Jusin, J.; Jaafar, J.; Aziz, M.; Ismail, A.F.; Othman, M.H.D.; Abd Rahman, M.; Aziz, F.; Yusof, N.; et al. Tuning the Oxygen Functional Groups in Graphene Oxide Nanosheets by Optimizing the Oxidation Time. *Phys. E Low. Dimens. Syst. Nanostr.* **2021**, *131*, 114727. [CrossRef]
91. Khan, M.; Tahir, M.N.; Adil, S.F.; Khan, H.U.; Siddiqui, M.R.H.; Al-Warthan, A.A.; Tremel, W. Graphene Based Metal and Metal Oxide Nanocomposites: Synthesis, Properties and Their Applications. *J. Mater. Chem. A Mater.* **2015**, *3*, 18753–18808. [CrossRef]
92. Ganesha, H.; Veeresh, S.; Nagaraju, Y.S.; Suresh, D.S.; Vijaykumar, S.P.; Sapna, S.; Khmis, A.; Devendrappa, H. Polymer Incorporated with Graphene Oxide Composite for High Electrochemical Performance. *Mater. Today Proc.* **2023**. [CrossRef]
93. Bai, H.; Li, C.; Shi, G. Functional Composite Materials Based on Chemically Converted Graphene. *Adv. Mater.* **2011**, *23*, 1089–1115. [CrossRef]
94. Seok, D.; Jeong, Y.; Han, K.; Yoon, D.Y.; Sohn, H. Recent Progress of Electrochemical Energy Devices: Metal Oxide-Carbon Nanocomposites as Materials for next-Generation Chemical Storage for Renewable Energy. *Sustainability* **2019**, *11*, 3694. [CrossRef]
95. Kochaev, A.I.; Efimov, V.V.; Kaya, S.; Flores-Moreno, R.; Katin, K.P.; Maslov, M.M. On Point Perforating Defects in Bilayer Structures. *Phys. Chem. Chem. Phys.* **2023**, *25*, 30477–30487. [CrossRef]
96. Mbayachi, V.B.; Ndayiragije, E.; Sammani, T.; Taj, S.; Mbuta, E.R.; Ullah Khan, A. Graphene Synthesis, Characterization and Its Applications: A Review. *Results Chem.* **2021**, *3*, 100163. [CrossRef]
97. Sun, X.; Sun, H.; Li, H.; Peng, H. Developing Polymer Composite Materials: Carbon Nanotubes or Graphene? *Adv. Mater.* **2013**, *25*, 5153–5176. [CrossRef]
98. Saeed, K.; Khan, I.; Khan, I.; Ali, N.; Bilal, M.; Akhter, M.S. Graphene and Carbon Nanotubes-Based Polymer Nanocomposites. In *Smart Polymer Nanocomposites*; Elsevier: Amsterdam, The Netherlands, 2023; pp. 205–218.
99. Wang, J.; Zhang, Y.; Liu, G.; Zhang, T.; Zhang, C.; Zhang, Y.; Feng, Y.; Chi, Q. Improvements in the Magnesium Ion Transport Properties of Graphene/CNT-Wrapped TiO_2-B Nanoflowers by Nickel Doping. *Small* **2023**, 2304969. [CrossRef]
100. Sonkar, P.K.; Ganesan, V.; Sen Gupta, S.K.; Yadav, D.K.; Gupta, R.; Yadav, M. Highly Dispersed Multiwalled Carbon Nanotubes Coupled Manganese Salen Nanostructure for Simultaneous Electrochemical Sensing of Vitamin B2 and B6. *J. Electroanal. Chem.* **2017**, *807*, 235–243. [CrossRef]
101. Lu, B.; Zhang, Z.; Hao, J.; Xu, G.; Zhang, B.; Tang, J. Electrochemical Sensing Platform Based on Schiff-Base Cobalt(Ii)/Single-Walled Carbon Nanohorns Complexes System. *Anal. Methods* **2012**, *4*, 3580–3585. [CrossRef]
102. Rajarao, R.; Kim, T.H.; Bhat, B.R. Multi-Walled Carbon Nanotube Bound Nickel Schiff-Base Complexes as Reusable Catalysts for Oxidation of Alcohols. *J. Coord. Chem.* **2012**, *65*, 2671–2682. [CrossRef]
103. Salavati-Niasari, M.; Bazarganipour, M. Covalent Functionalization of Multi-Wall Carbon Nanotubes (MWNTs) by Nickel(II) Schiff-Base Complex: Synthesis, Characterization and Liquid Phase Oxidation of Phenol with Hydrogen Peroxide. *Appl. Surf. Sci.* **2008**, *255*, 2963–2970. [CrossRef]

104. Bai, L.; Li, M.; Guan, J. Co(II) or Cu(II) Schiff Base Complex Immobilized onto Carbon Nanotubes as a Synergistic Catalyst for the Oxygen Reduction Reaction. *ChemistrySelect* **2018**, *3*, 581–585. [CrossRef]
105. Li, H.; Zhong, M.; Li, C.; Ren, Y.; Chen, J.; Yang, Q. Synthesis of CNTs@POP-Salen Core-Shell Nanostructures for Catalytic Epoxides Hydration. *ChemCatChem* **2019**, *11*, 3952–3958. [CrossRef]
106. Zheng, W.; Tan, R.; Yin, S.; Zhang, Y.; Zhao, G.; Chen, Y.; Yin, D. Ionic Liquid-Functionalized Graphene Oxide as an Efficient Support for the Chiral Salen Mn(iii) Complex in Asymmetric Epoxidation of Unfunctionalized Olefins. *Catal. Sci. Technol.* **2015**, *5*, 2092–2102. [CrossRef]
107. Zhou, X.; Lu, X. Co(Salen) Supported on Graphene Oxide for Oxidation of Lignin. *J. Appl. Polym. Sci.* **2016**, *133*, 44133. [CrossRef]
108. Li, Z.; Wu, S.; Ding, H.; Lu, H.; Liu, J.; Huo, Q.; Guan, J.; Kan, Q. Oxovanadium(Iv) and Iron(Iii) Salen Complexes Immobilized on Amino-Functionalized Graphene Oxide for the Aerobic Epoxidation of Styrene. *New J. Chem.* **2013**, *37*, 4220–4229. [CrossRef]
109. Wei, W.-C.; Deng, C.; Huang, S.-C.; Wei, Y.-X.; Wang, Y.-Z. Nickel-Schiff Base Decorated Graphene for Simultaneously Enhancing the Electroconductivity, Fire Resistance, and Mechanical Properties of a Polyurethane Elastomer. *J. Mater. Chem. A Mater.* **2018**, *6*, 8643–8654. [CrossRef]
110. Li, Z.; Wu, S.; Ding, H.; Zheng, D.; Hu, J.; Wang, X.; Huo, Q.; Guan, J.; Kan, Q. Immobilized Cu(Ii) and Co(Ii) Salen Complexes on Graphene Oxide and Their Catalytic Activity for Aerobic Epoxidation of Styrene. *New J. Chem.* **2013**, *37*, 1561–1568. [CrossRef]
111. Zhao, Q.; Bai, C.; Zhang, W.; Li, Y.; Zhang, G.; Zhang, F.; Fan, X. Catalytic Epoxidation of Olefins with Graphene Oxide Supported Copper (Salen) Complex. *Ind. Eng. Chem. Res.* **2014**, *53*, 4232–4238. [CrossRef]
112. Ghabdian, M.; Nasseri, M.A.; Allahresani, A.; Motavallizadehkakhky, A. Heterogenized Cu (II) Salen Complex Grafted on Graphene Oxide Nanosheets as a Precursing Catalyst for the Pd-free Sonogashira Coupling. *Appl. Organomet. Chem.* **2018**, *32*, 4545:1–4545:9. [CrossRef]
113. Li, X.; Xu, G.; Deng, F.; Chen, C.; Li, J.; Kang, F. Understanding the Charge Storage Mechanism and Electrochemical Performance on the Poly[Ni(Salen)]-Modified Electrode Electropolymerized with Different Sweep Rate. *Electrochemistry* **2017**, *85*, 461–468. [CrossRef]
114. Araújo, M.P.; Nunes, M.; Fonseca, J.; Moura, C.; Hillman, R.; Freire, C. Graphene-Poly(Nickel Complex) as Novel Electrochromic Nanocomposite for the Fabrication of a Robust Solid-State Device. *J. Colloid. Interface Sci.* **2017**, *504*, 790–799. [CrossRef]
115. Karushev, M.P.; Timonov, A.M. Adsorption-Electrochemical Modification of Nanoporous Carbon Materials by Nickel Complexes with Schiff Bases. *Russ. J. Appl. Chem.* **2012**, *85*, 914–920. [CrossRef]
116. Gao, F.; Li, J.; Kang, F.; Zhang, Y.; Wang, X.; Ye, F.; Yang, J. Preparation and Characterization of a Poly[Ni(Salen)]/Multiwalled Carbon Nanotube Composite by in situ Electropolymerization as a Capacitive Material. *J. Phys. Chem. C* **2011**, *115*, 11822–11829. [CrossRef]
117. Hüfner, S. *Photoelectron Spectroscopy*; Springer Series in Solid-State Sciences; Springer: Berlin/Heidelberg, Germany, 1995; Volume 82, ISBN 978-3-662-03152-0.
118. Korusenko, P.; Kharisova, K.; Knyazev, E.; Levin, O.; Vinogradov, A.; Alekseeva, E. Surface Engineering of Multi-Walled Carbon Nanotubes via Ion-Beam Doping: Pyridinic and Pyrrolic Nitrogen Defect Formation. *Appl. Sci.* **2023**, *13*, 11057. [CrossRef]
119. Shunaev, V.V.; Bobenko, N.G.; Korusenko, P.M.; Egorushkin, V.E.; Glukhova, O.E. Carboxyl Functionalization of N-MWCNTs with Stone–Wales Defects and Possibility of HIF-1α Wave-Diffusive Delivery. *Int. J. Mol. Sci.* **2023**, *24*, 1296. [CrossRef]
120. Tanuma, S.; Powell, C.J.; Penn, D.R. Calculations of Electron Inelastic Mean Free Paths. IX. Data for 41 Elemental Solids over the 50 EV to 30 KeV Range. *Surf. Interface Anal.* **2011**, *43*, 689–713. [CrossRef]
121. Fairley, N.; Fernandez, V.; Richard-Plouet, M.; Guillot-Deudon, C.; Walton, J.; Smith, E.; Flahaut, D.; Greiner, M.; Biesinger, M.; Tougaard, S.; et al. Systematic and Collaborative Approach to Problem Solving Using X-ray Photoelectron Spectroscopy. *Appl. Surf. Sci. Adv.* **2021**, *5*, 100112. [CrossRef]
122. Yeh, J.J.; Lindau, I. Atomic Subshell Photoionization Cross Sections and Asymmetry Parameters: $1 \leq Z \leq 103$. *At. Data Nucl. Data Tables* **1985**, *32*, 1–155. [CrossRef]
123. Yan, M.; Jin, Y.; Wu, Z.; Tsaturyan, A.; Makarova, A.; Smirnov, D.; Voloshina, E.; Dedkov, Y. Correlations in the Electronic Structure of van Der Waals $NiPS_3$ Crystals: An X-ray Absorption and Resonant Photoelectron Spectroscopy Study. *J. Phys. Chem. Lett.* **2021**, *12*, 2400–2405. [CrossRef] [PubMed]
124. Jin, Y.; Yan, M.; Kremer, T.; Voloshina, E.; Dedkov, Y. Mott–Hubbard Insulating State for the Layered van Der Waals FePX3 (X: S, Se) as Revealed by NEXAFS and Resonant Photoelectron Spectroscopy. *Sci. Rep.* **2022**, *12*, 735. [CrossRef] [PubMed]
125. Dedkov, Y.S.; Vinogradov, A.S.; Fonin, M.; König, C.; Vyalikh, D.V.; Preobrajenski, A.B.; Krasnikov, S.A.; Kleimenov, E.Y.; Nesterov, M.A.; Rüdiger, U.; et al. Correlations in the Electronic Structure of Half-Metallic Ferromagnetic CrO_2 Films: An X-ray Absorption and Resonant Photoemission Spectroscopy Study. *Phys. Rev. B* **2005**, *72*, 060401. [CrossRef]
126. Stöhr, J. *NEXAFS Spectroscopy*; Springer Series in Surface Sciences; Springer: Berlin/Heidelberg, Germany, 1992; Volume 25, ISBN 978-3-642-08113-2.
127. Vinogradov, A.S.; Fedoseenko, S.I.; Krasnikov, S.A.; Preobrajenski, A.B.; Sivkov, V.N.; Vyalikh, D.V.; Molodtsov, S.L.; Adamchuk, V.K.; Laubschat, C.; Kaindl, G. Low-Lying Unoccupied Electronic States in 3d Transition-Metal Fluorides Probed by NEXAFS at the F1s Threshold. *Phys. Rev. B* **2005**, *71*, 045127:1–045127:11. [CrossRef]
128. Newville, M. Fundamentals of XAFS. *Rev. Miner. Geochem.* **2014**, *78*, 33–74. [CrossRef]
129. Zubavichus, Y.V.; Slovokhotov, Y.L. X-ray Synchrotron Radiation in Physicochemical Studies. *Russ. Chem. Rev.* **2001**, *70*, 373–403. [CrossRef]

130. Borovskiĭ, I.B.; Vedrinskiĭ, R.V.; Kraĭzman, V.L.; Sachenko, V.P. EXAFS Spectroscopy: A New Method for Structural Investigation. *Sov. Phys. Uspekhi* **1986**, *29*, 539–569. [CrossRef]
131. Sanson, A. EXAFS Spectroscopy: A Powerful Tool for the Study of Local Vibrational Dynamics. *Microstructures* **2021**, *1*, 2021004. [CrossRef]
132. Penner-Hahn, J.E. X-ray Absorption Spectroscopy. In *Comprehensive Coordination Chemistry II*; Elsevier: Amsterdam, The Netherlands, 2003; pp. 159–186.
133. Newville, M. IFEFFIT: Interactive XAFS Analysis and FEFF Fitting. *J. Synchrotron Radiat.* **2001**, *8*, 322–324. [CrossRef] [PubMed]
134. Salavati-Niasari, M.; Mirsattari, S.N.; Bazarganipour, M. Synthesis, Characterization and Catalytic Oxyfunctionalization of Cyclohexene with Tert-Butylhydroperoxide over a Manganese(II) Complex Covalently Anchored to Multi-Wall Carbon Nanotubes (MWNTs). *Polyhedron* **2008**, *27*, 3653–3661. [CrossRef]
135. Salavati-Niasari, M.; Bazarganipour, M. Synthesis, Characterization and Alcohol Oxidation Properties of Multi-Wall Carbon Nanotubes Functionalized with a Cobalt(II) Schiff Base Complex. *Transit. Metal. Chem.* **2009**, *34*, 605–612. [CrossRef]
136. Ghadamyari, Z.; Khojastehnezhad, A.; Seyedi, S.M.; Taghavi, F.; Shiri, A. Graphene Oxide Functionalized Zn(II) Salen Complex: An Efficient and New Route for the Synthesis of 1,2,3-Triazole Derivatives. *ChemistrySelect* **2020**, *5*, 10233–10242. [CrossRef]
137. Salavati-Niasari, M.; Bazarganipour, M. Synthesis, Characterization and Catalytic Oxidation Properties of Multi-Wall Carbon Nanotubes with a Covalently Attached Copper(II) Salen Complex. *Appl. Surf. Sci.* **2009**, *255*, 7610–7617. [CrossRef]
138. Salavati-Niasari, M.; Bazarganipour, M. Synthesis, Characterization and Liquid Phase Oxidation of Cyclohexane with Hydrogen Peroxide over Oxovanadium(IV) Schiff-Base Tetradendate Complex Covalently Anchored to Multi-Wall Carbon Nanotubes (MWNTs). *Bull. Korean Chem. Soc.* **2009**, *30*, 355–362. [CrossRef]
139. Zhang, M.; Zhao, F.; Li, H.; Yuan, Z.; Dong, S.; Wang, Y.; Chen, X.; Yang, Y.; Song, X.; Jiang, Z. Insight into Graphene-Salen Metal Nanocomposites on Combustion Performance and Mechanism of HMX-CMDB Propellant. *Chem. Eng. J.* **2022**, *429*, 132175. [CrossRef]